Magnetic and transport properties of the layered transition-metal pnictides $R_3T_4As_4O_{2-\delta}$ (R = La, Ce, Pr, Nd, and Sm, T = Ni, Cu)

Jiakui K. Wang,[1] A. Marcinkova,[1] Chih-Wei Chen,[1] Hua He,[2] Meigan Aronson,[2,3] and E. Morosan[1]

[1]*Department of Physics and Astronomy, Rice University, Houston, Texas 77005, USA*

[2]*Department of Physics and Astronomy, Stony Brook University, Stony Brook, New York 11794, USA*

[3]*Condensed Matter Physics and Materials Science Department, Brookhaven National Laboratory, Upton, New York 11973, USA*

(Received 4 November 2013; revised manuscript received 12 February 2014; published 6 March 2014)

The magnetic and transport properties of the novel $R_3T_4As_4O_{2-\delta}$ (R = La, Ce, Pr, Nd and Sm, T = Ni and Cu) layered materials were studied using structural and physical properties measurements. Varying the rare-earth ion led to the observation of diverse physical properties including superconductivity for R = La and T = Ni, ferromagnetic or antiferromagnetic order for R = Ce, Pr, and Sm, or spin-glass behavior in $Nd_3Ni_4As_4O_{2-\delta}$. These complex magnetic and electronic properties are discussed in light of the crystalline anisotropy in these layered compounds.

DOI: 10.1103/PhysRevB.89.094405 PACS number(s): 75.30.−m, 74.10.+v, 75.50.Lk, 75.47.−m

I. INTRODUCTION

Intensive research interest on layered transition-metal pnictides was stimulated by the discovery of high-temperature superconductivity in Fe-pnictides and chalcogenides a few years ago [1,2]. A widely debated problem brought about by this discovery concerns the relationship between the structure, magnetism, and superconductivity in Fe-X (X = pnictogen or chalcogen) and other families of unconventional superconductors. While 3d electrons often show itinerant local moment duality, it is the local crystalline environment that drastically influences the magnetic ground state of the transition-metal ions. The properties of 3d electrons are susceptible to perturbations from chemical doping, magnetic field, or pressure [3–8], and complex physics such as unconventional superconductivity often emerges at the local-to-itinerant electron-state crossover [9,10]. Therefore, the crystal structure, magnetism, and superconductivity are intimately related as a result of the dual nature of the 3d electrons.

In the known layered Fe-X compounds, an edge-sharing tetrahedral structure formed by the Fe and X ions is thought to be responsible for the itinerant magnetism [10]. Due to the relatively close Fe and X electronegativities, the bonds between the anion and cation tend to be metallic covalent and weak. At low temperature, those compounds order antiferromagnetically via a spin density wave transition in these layered structures, and the magnetism can be suppressed with chemical doping or pressure, in favor of unconventional superconductivity.

While many Fe-based superconductors have been discovered in recent years, they generally have one or two Fe-X functional layers within the unit cell [11–14]. It is thus of interest to know whether more functional layers in the unit cell would be beneficial for superconductivity, similar to what had been seen in cuprates [15]. The $R_3Cu_4P_4O_{2-\delta}$ (3442) family of layered transition-metal pnictides, previously reported in Ref. [16], represents one such multilayer structure. The 3442 structure is a convolution of the functional layers and different blocking layers from the known RFeXO (1111) and $BaFe_2As_2$ (122) families of pnictides (Fig. 1). The similarities between the $R_3Cu_4P_4O_{2-\delta}$ and the superconducting Fe-X compounds include the highly anisotropic unit cell, the edge-shared tetrahedral layers formed by T and X (T = transition metal), and the metallic transport properties. These similarities might be further enhanced if Cu could be replaced by Fe in $R_3Cu_4X_4O_{2-\delta}$, to form FeX tetrahedral layers, identical to those in the known Fe-based superconductors. However, the stability of 1111 and 122 phases makes synthesizing the 3442 Fe equivalent compounds difficult.

This study is a report of the structural and physical properties of the newly synthesized compounds $R_3T_4As_4O_{2-\delta}$ (R = La, Ce, Pr, Nd, and Sm, T = Ni, Cu). By varying the R and T, the structural, magnetic, and transport properties vary, with a wide range of ground states, from superconductivity (for R = La and T = Ni) to long-range magnetic order (for R = Ce, Pr, Sm and T = Cu, Ni) or spin glass (for R = Nd and T = Ni). Understanding the physical properties of the many compounds in such a family presents a potential for in-depth insight into the relation between the crystallographical structure, magnetic configuration, and superconductivity. In turn, such insight may allow for the design of higher-temperature superconductors with multiple functional layers.

II. EXPERIMENTAL METHODS

Polycrystalline samples of $R_3T_4As_4O_{2-\delta}$ (R = La, Ce, Pr, Nd, and Sm, T = Ni, Cu) were synthesized by solid-state reaction, with initial compositions R:Cu_2O:As = 3:2:4 or R:NiO:Ni:As = 3:2:2:4. The alumina crucible containing the starting materials was sealed under vacuum in a silica tube. The heating recipes consisted of three steps, and were slightly different for each compound. In the first step, the mixture was heated for 7 days at several temperatures between 450 °C and 950 °C. Following an intermediate grinding, the samples were reannealed at temperatures between 1000 °C and 1100 °C for 3 days. For the third and last step, the powders were pressed into pellets and reannealed at the maximum temperature from step 2. Refinements of the x-ray diffraction (XRD) data suggest possible oxygen deficiency, resulting in the stoichiometry $R_3T_4As_4O_{2-\delta}$. The oxygen deficiency δ in $R_3T_4As_4O_{2-\delta}$ can not be accurately determined from powder XRD data alone. However, it appears to be a general feature in these 3442 systems, as it was also reported in the phosphorus analogs [17].

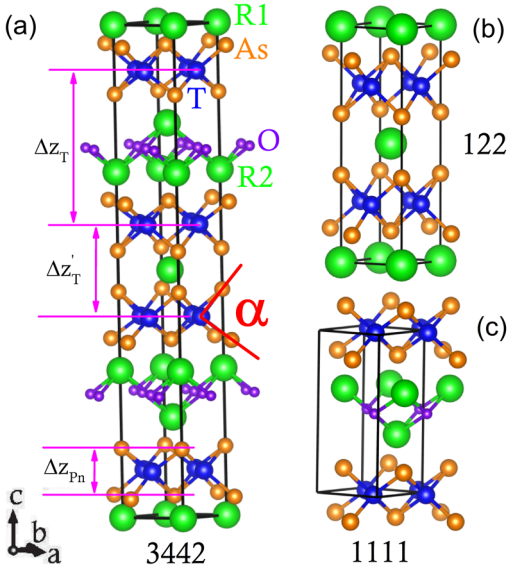

FIG. 1. (Color online) Comparison of the crystal structures of (a) 3442 (space group $I4/mmm$), (b) 122 (space group $I4/mmm$), and (c) 1111 (space group $P4/nmm$) compounds. The 3442 unit cell can be viewed as a combination of the 1111 and 122 unit cells. Rare-earth, oxygen, transition-metal, and arsenic atoms are depicted in green, red, blue, and orange. Δz_T ($\Delta z'_T$) represent the distance between adjacent T-Pn layers sandwiching $R2$ ($R1$), and Δz_{Pn} is the distance between Pn planes above and below the same T plane, respectively.

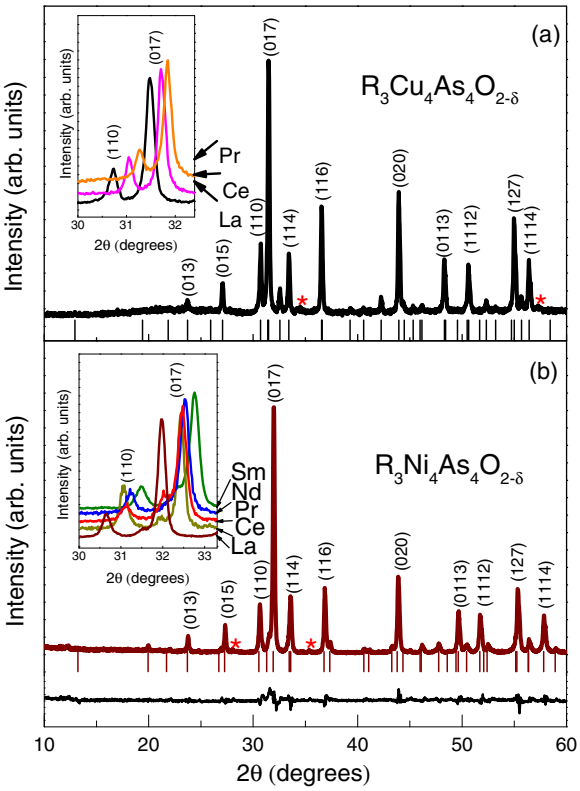

FIG. 2. (Color online) X-ray diffraction patterns for $R_3T_4As_4O_{2-\delta}$ for (a) T = Cu and R = La, Ce, Pr, and (b) T = Ni and R = La, Ce, Pr, Nd, and Sm, with the calculated peak positions (vertical lines) for $La_3T_4As_4O_{2-\delta}$ and the difference between measured and calculated intensity for $La_3Ni_4As_4O_{2-\delta}$ (bottom). Inset: detailed view around the (015) and (017) peaks, illustrating the peak shift across the respective T series. Impurity peaks in these compounds are marked by asterisks.

Figure 2 illustrates the powder x-ray diffraction patterns for (a) $La_3Cu_4As_4O_{2-\delta}$ and (b) $La_3Ni_4As_4O_{2-\delta}$, while the insets show details around the most intense peaks for all compounds in the two series reported here. Minor impurity phases were also revealed by XRD refinement, and the appropriate peaks are marked by asterisks in Fig. 2.

Magnetization measurements up to 300 K were performed in a Quantum Design (QD) Magnetic Property Measurement System (MPMS). The specific heat, dc or ac resistivity, and ac magnetization were measured in a QD Physical Property Measurement System (PPMS). Phase analysis was done using laboratory powder x-ray diffraction on a Rigaku D/max diffractometer with a Cu $K\alpha$ radiation source. Rietveld analysis of the collected powder XRD data was performed using the GSAS software package [18].

III. RESULTS

The room-temperature (RT) crystal structure of the $R_3T_4As_4O_2$ is shown in Fig. 1. Rietveld analysis confirms that the $I4/mmm$ space group describes all new $R_3T_4As_4O_{2-\delta}$ compounds (T = Cu, R = La, Ce, Pr; and T = Ni, R = La, Ce, Pr, Nd, Sm) reported here. The RT lattice parameters for these compounds are listed in Table I. For T = Cu, they appear to be significantly larger compared to those of the phosphorus analogs $R_3Cu_4P_4O_2$ (R = La, Ce, Pr, Nd, and Sm) [16,17]. This can be simply explained by negative chemical pressure when smaller P (with ionic radius $r_P \approx 0.44$ Å) is replaced by As (with a larger ionic radius $r_{As} \approx 0.58$ Å) [19]. As expected, the lattice parameters across the $R_3Cu_4As_4O_{2-\delta}$ (R = La, Ce, Pr) and $R_3Ni_4As_4O_{2-\delta}$ (R = La, Ce, Pr, Nd, and Sm) series decrease with decreasing R ionic size.

The transition-metal T ions (blue in Fig. 1) form a square planar net, with the T-T bond distance decreasing in $R_3Cu_4As_4O_{2-\delta}$ from $d_{Cu\text{-}Cu}$ = 2.9184(2) Å for R = La, to 2.8770(5) Å for R = Pr. In all cases, the $d_{Cu\text{-}Cu}$ distance is larger than the corresponding values reported in the phosphorus analogs [16]. The same trend is observed in $R_3Ni_4As_4O_{2-\delta}$, in which the $d_{Ni\text{-}Ni}$ bond distance decreases from $d_{Ni\text{-}Ni}$ = 2.8879(2) Å for R = La to 2.8392(3) Å for R = Sm, but it is still larger than that in $La_3Ni_4P_4O_2$ [20].

Each T ion is tetrahedrally coordinated by As atoms, resulting in TAs_4 tetrahedral planes, similar to the T-Pn planes in the 122 and 1111 superconductors [Figs. 1(b) and 1(c)]. Decreasing the R size leads to a decrease of α, the As-T-As angle [marked in Fig. 1(a)] in both T = Cu and Ni $R_3T_4As_4O_{2-\delta}$ series: for T = Cu, α decreases from 116.16(2)° for R = La to 113.59(2)° for R = Pr. In $R_3Ni_4As_4O_{2-\delta}$, α is overall much larger than in the T = Cu series, and it decreases from α = 120.96(3)° for R = La to α = 118.7(5)° for R = Sm. Surprisingly, for $La_2PrNi_4As_4O_{2-\delta}$ α is 122.85(6)°, larger than that for $La_3Ni_4As_4O_{2-\delta}$, even though the lattice parameters were, as expected, smaller in the former compound a = 4.010 Å, c = 26.497 Å. However, in $LaPr_2Ni_4As_4O_{2-\delta}$,

TABLE I. Structural parameters and purity information for $R_3Cu_4As_4O_{2-\delta}$ (R = La–Pr) and $R_3Ni_4As_4O_{2-\delta}$ (R = La–Sm), estimated from powder x-ray diffraction.

Transition metal (T)	Cu			Ni						
Rare earth (R)	La	Ce	Pr	La	Ce	Pr	Nd	Sm	$(La_2Pr)_{1/3}$	$(LaPr_2)_{1/3}$
a (Å)	4.1247(4)	4.0713(4)	4.0652(8)	4.1146(1)	4.0760(3)	4.0649(6)	4.0473(3)	4.0152(4)	4.0998(5)	4.0838(4)
c (Å)	27.557(3)	27.391(3)	27.436(6)	26.594(1)	26.309(2)	26.2603(4)	26.2250(2)	26.0590(3)	26.4970(4)	26.3740
Volume (Å^3)	468.831	454.019	453.403	450.235	437.092	433.910	429.582	420.119	445.371	439.850
Purity (wt %)	95	97	90	97	95	89	98	96.5	98	99
$\Delta z_T/\Delta z_{Pn}$	3.17	3.14	3.11	3.44	3.31	3.45	3.30	3.27	3.41	3.37
$\Delta z'_T/\Delta z_{Pn}$	2.01	2.01	2.01	2.12	2.06	2.11	2.07	2.01	2.10	2.09

α is 119.99(3)°, commensurate with the expected lanthanide contraction, and consistent with the experimental lattice parameters $a = 4.084$ Å and $c = 26.374$ Å. Furthermore, from the XRD refinements on $La_xPr_{3-x}Ni_4As_4O_{2-\delta}$ samples, in $x = 1$, La occupies the $R1$ site (i.e., the site without neighboring O), while for $x = 2$, the La fully occupies the $R1$ site and partially the $R2$ site (i.e., the site with neighboring O). As will be shown in the following, $La_3Ni_4As_4O_{2-\delta}$ is superconducting below $T_c = 2$ K, while none of the other compounds reported here are superconducting above 0.4 K. This is consistent with the trends reported for the T = Ni 122 and 1111 series [21], where T_c increased as α was further away from the ideal tetrahedral angle $\alpha_{ideal} = 109.5°$.

The powder x-ray refinements indicate that the purity of the $R_3Cu_4As_4O_{2-\delta}$ (R = La, Ce) and $R_3Ni_4As_4O_{2-\delta}$ (R = La, Ce, Nd, and Sm) samples is higher than 95%, while the Pr compounds in both T = Ni, Cu series had slightly lower purity, ∼90%. To extract the impurity fractions in $R_3T_4As_4O_{2-\delta}$ (R = Pr, T = Ni, Cu), the phase fraction scale factors were fixed, and then changed manually until the goodness of the Rietveld fits converged to the minimal values, and the impurity peaks were properly fit. This procedure was necessary due to the overlap of the most intense peak of the PrCu and NiAs secondary phases with a (110) Bragg peak of the 3442 main phase. This procedure was done for all $R_3T_4As_4O_{2-\delta}$ samples, for consistency. From all detectable impurity phases, PrCu, Nd_2O_3, $CeNi_2As_2$, and Pr_2NiO_4 are magnetic [22–25]. While the former two impurities show no magnetic phase transition down to 2 K, the latter two show antiferromagnetic phase transitions at 4.8 and 325 K, respectively. These transitions are not visible in the $Ce_3Ni_4As_4O_{2-\delta}$ or $Pr_3Ni_4As_4O_{2-\delta}$ samples in this study (for which the respective impurity phases were detected), indicating that their measured properties are intrinsic.

A. $Ce_3Cu_4As_4O_{2-\delta}$

The temperature-dependent inverse susceptibility H/M of $R_3Cu_4As_4O_{2-\delta}$ (R = Ce) for $H = 0.1$ T is shown in Fig. 3, with the low temperature M/H displayed in the inset for R = Ce (squares) and La (diamonds). Curie-Weiss behavior is observed for $Ce_3Cu_4As_4O_{2-\delta}$ above 100 K as $H/(M\text{-}M_0)$ is linear in temperature up to 700 K, after subtracting a temperature-independent constant $M_0/H \approx 2.6 \times 10^{-4}$ emu/mol$_{Ce}$. From the linear fit of $H/(M\text{-}M_0)$ above 100 K, a negative Weiss temperature $\theta_W \approx -8$ K is determined, indicative of antiferromagnetic coupling. The effective moment $\mu_{eff} = 2.04\,\mu_B/Ce^{3+}$ is smaller but close to the theoretical value $\mu_{eff}^{th} = 2.54\ \mu_B/Ce^{3+}$, or the value $2.33\,\mu_B/Ce^{3+}$ for $Ce_3Cu_4P_4O_{2-\delta}$ [16]. These observations are consistent with Cu being nonmagnetic below ∼700 K, and Ce ions being in a 3+ oxidation state. Further indication of Cu being nonmagnetic is provided by the $M(T)$ data on the La analog (diamonds, inset, Fig. 3) for which a small paramagnetic (∼10^{-4} emu/mol$_{La}$), non-Curie-Weiss signal is registered. At low temperatures, the temperature-dependent magnetization for $Ce_3Cu_4As_4O_{2-\delta}$, together with neutron diffraction data [26], reveals two transitions around 30 and 10 K (inset, Fig. 3), associated with short-range magnetic correlations. The divergence of the zero-field-cooled (ZFC) and field-cooled (FC) data below 30 K is indicative of a small ferromagnetic component of the magnetization.

The magnetic ground state revealed by $M(T)$ above is consistent with the field dependence of the $R_3Cu_4As_4O_{2-\delta}$ magnetization at $T = 2$ K, shown in Fig. 4 for R = Ce (squares) and La (diamonds). As is readily apparent from

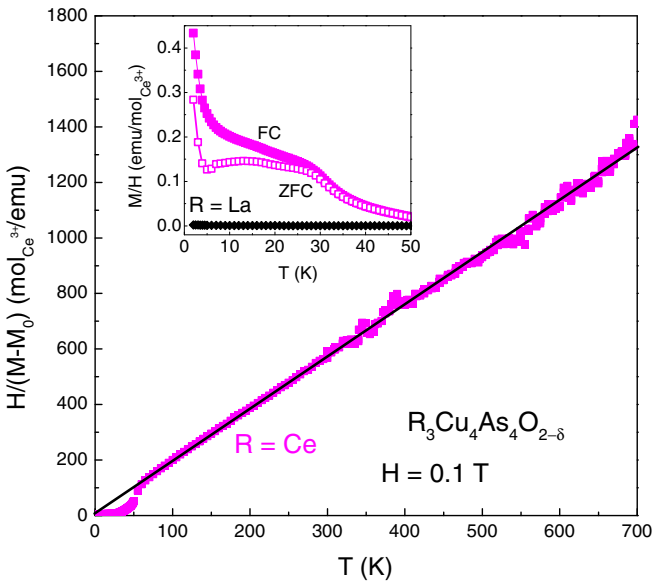

FIG. 3. (Color online) The temperature-dependent inverse susceptibility $H/(M\text{-}M_0)$ of $Ce_3Cu_4As_4O_{2-\delta}$ for $H = 0.1$ T. The solid line is the extrapolated linear fit of $H/(M\text{-}M_0)$ above 50 K. Inset: the low-temperature ZFC (open) and FC (full symbols) M/H for $Ce_3Cu_4As_4O_{2-\delta}$ (squares) and for $La_3Cu_4As_4O_{2-\delta}$ (diamonds).

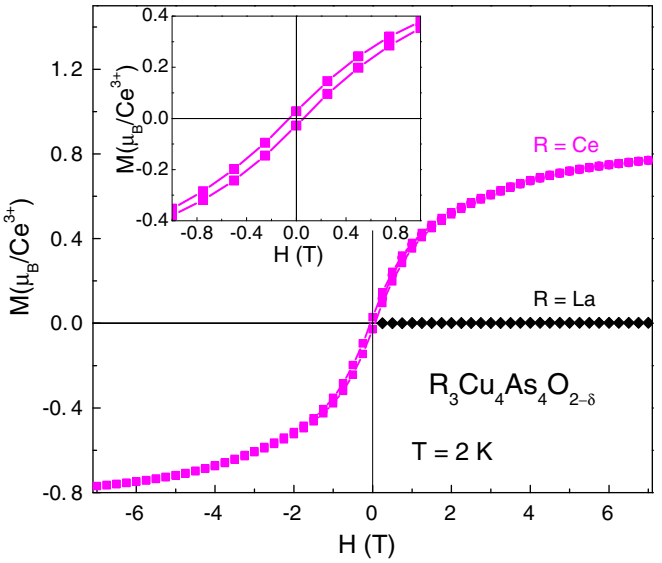

FIG. 4. (Color online) The magnetization isotherms at $T = 2$ K for $Ce_3Cu_4As_4O_{2-\delta}$ (squares) and for $La_3Cu_4As_4O_{2-\delta}$ (diamonds). Inset: detailed view of magnetization isotherms in the low-field region.

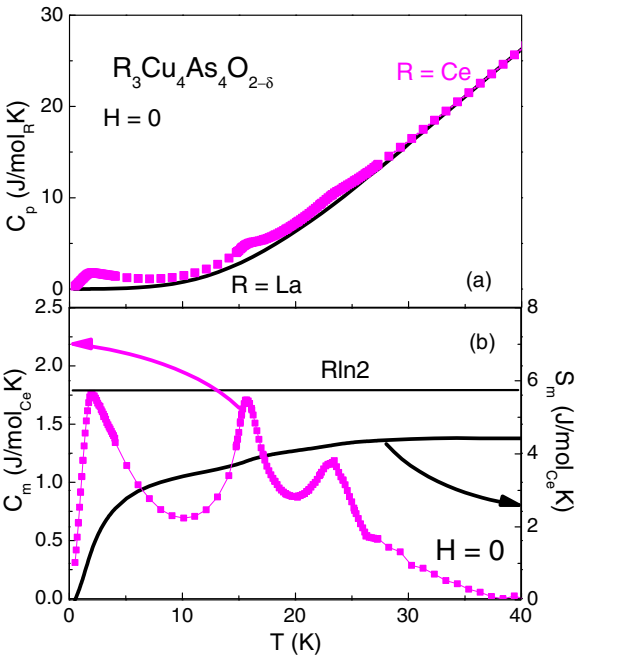

FIG. 5. (Color online) (a) The specific heat of $R_3Cu_4As_4O_{2-\delta}$ for $R =$ Ce (symbols) and $R =$ La (line) for $H = 0$. (b) The magnetic specific heat C_m (symbols, left axis) and the magnetic entropy S_m (line, right axis).

the inset, both the residual magnetization and the coercive field for $Ce_3Cu_4As_4O_{2-\delta}$ are very small, consistent with antiferromagnetic moment coupling with a small ferromagnetic component. Indeed, the 3442 crystal structure (Fig. 1) suggests the interlayer coupling to be much smaller than the intralayer coupling, given that the distances between adjacent T-As layers $\Delta z_T(\Delta z'_T)$, normalized by the T-As layer thickness Δz_{Pn}, are $\Delta z_T/\Delta z_{Pn} \sim 3.14$ and $\Delta z'_T/\Delta z_{Pn} \sim 2.01$, comparable with the values 3.31 in LaOFeAs [1] and 2.08 in $BaFe_2As_2$ [2], respectively. For comparison, $\Delta z_T(\Delta z'_T)/\Delta z_{Pn}$ are also calculated for all the compounds $T =$ Cu and $T =$ Ni series as shown in Table I. Decreasing $\Delta z_T(\Delta z'_T)/\Delta z_{Pn}$ is in good agreement with the expected trend, i.e., with decreasing c lattice parameter from $R =$ La to Sm the thickness of the T-As layer decreases, as does the height of the As ion. In $Pr_3Ni_4As_4O_{2-\delta}$, the average $\Delta z_T(\Delta z'_T)/\Delta z_{Pn}$ is higher than that of $R =$ La and Ce, possibly due to the slightly higher impurity levels.

Preliminary neutron experiments on $Ce_3Ni_4As_4O_{2-\delta}$ [26], which indicate small Ce moment ordering, also converge towards a quasi-two-dimensional (quasi-2D) scenario as broad (00l) diffraction peaks suggest short interplane correlation lengths. Furthermore, the nonmagnetic nature of the Cu ions can be inferred both from neutron diffraction and from the very small $La_3Cu_4As_4O_{2-\delta}$ magnetization $M(H)$ (diamonds, Fig. 4). It should be noted that the magnetization for $R =$ Ce reaches only $\sim 0.8\ \mu_B/Ce^{3+}$ at the maximum applied field $H = 7$ T. This is about one third of the expected saturated moment $\mu_{sat}(Ce^{3+}) = 2.14\ \mu_B$, and is consistent with the neutrons' suggestion of small moment ordering. Another possible explanation may be that much larger fields are needed to reach saturation. Given the small $M(H)$ slope close to 7 T, the more plausible explanation could be drawn from crystal-field effects, also consistent with the quasi-2D picture from neutrons and crystallography.

Specific-heat measurements offer a complementary view into the magnetic properties of $Ce_3Cu_4As_4O_{2-\delta}$. The specific heat of $R_3Cu_4As_4O_{2-\delta}$, measured from 0.4 to 40 K, is shown in Fig. 5(a) for $R =$ Ce (symbols) and La (line). Three broad transitions are apparent for the Ce compound, around 1.9, 15.8, and 23.5 K, while no phase transition is observed for the La analog down to 0.4 K. The magnetic specific heat of $Ce_3Cu_4As_4O_{2-\delta}$, calculated as $C_m(\text{Ce}) = C_p(\text{Ce})\text{-}C_p(\text{La})$, is shown in Fig. 5(a) (symbols, left axis). The magnetic entropy $S_m(T) = \int_0^T dT'(C_m/T')$, shown in Fig. 5(a) (line, right axis), is close to R ln2 just above the transitions seen in C_m, consistent with a Kramers ground-state doublet. The broad peaks in C_p [Fig. 5(a)] become sharper in C_m [Fig. 5(b)], but are more akin to those associated with short-range correlations [27–29], a scenario also suggested by the above magnetization data and the ongoing neutron experiments [26].

The resistivity for $Ce_3Cu_4As_4O_{2-\delta}$ is shown in Fig. 6 for $H = 0$ (open squares) and 9 T (full squares), with that of $La_3Cu_4As_4O_{2-\delta}$ for $H = 0$ displayed in Fig. 7. $La_3Cu_4As_4O_{2-\delta}$ shows metallic behavior below 350 K (open diamonds), similar to $La_3Cu_4P_4O_{2-\delta}$ [16], but with resistivity values one to two orders of magnitude larger than those of the Ni analog (this study) or the P analog [16], and comparable with the resistivity of the Fe-pnictides superconductors [8]. A possible superconducting transition is present around 1.3 K (inset, Fig. 7), to be confirmed by further investigation. In stark contrast, in $Ce_3Cu_4As_4O_{2-\delta}$, resistivity increases slightly with decreasing temperature above 150 K, while below 50 K the system becomes metallic as the resistivity rapidly drops with decreasing temperature. The crossover from the high-temperature semiconducting to low-temperature metallic behavior occurs through a local maximum at intermediate

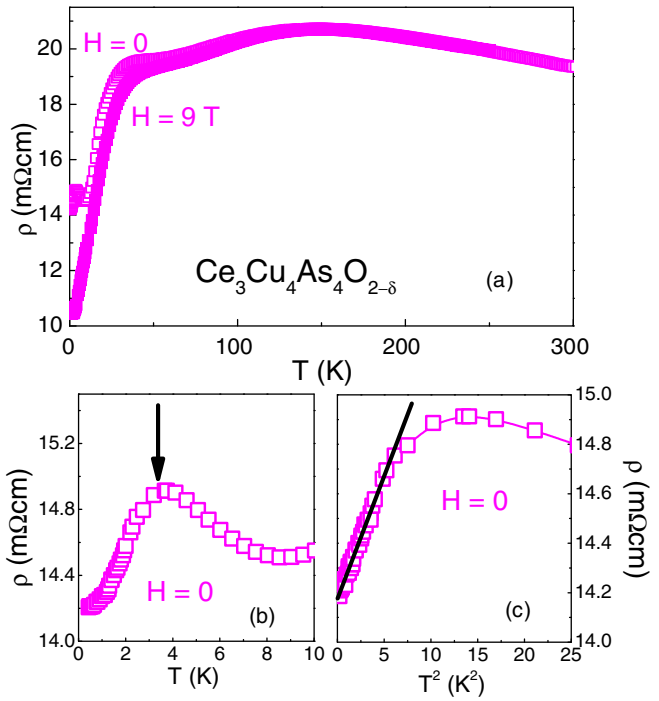

FIG. 6. (Color online) (a) The resistivity of $Ce_3Cu_4As_4O_{2-\delta}$ for $H = 0$ (open symbols) and 9 T (full symbols). (b) Low-temperature resistivity of $Ce_3Cu_4As_4O_{2-\delta}$, with a vertical arrow marking the low-temperature transition (see text). (c) Quadratic temperature dependence of the low-temperature resistivity for $Ce_3Cu_4As_4O_{2-\delta}$, with a solid line representing a fit below $T = 2.5$ K.

temperatures between ∼50 and 150 K. Another sharper local maximum is visible in the $H = 0$ $\rho(T)$ data around 4 K [vertical arrow, Fig. 6(b)]. It precedes the apparent Fermi liquid regime at low temperatures, suggested by the quadratic ρ in Fig. 6(c). This local temperature maximum, together with the low-temperature quadratic resistivity, is reminiscent of heavy-fermion behavior, where the competition between RKKY interaction and Kondo screening gives rise to such

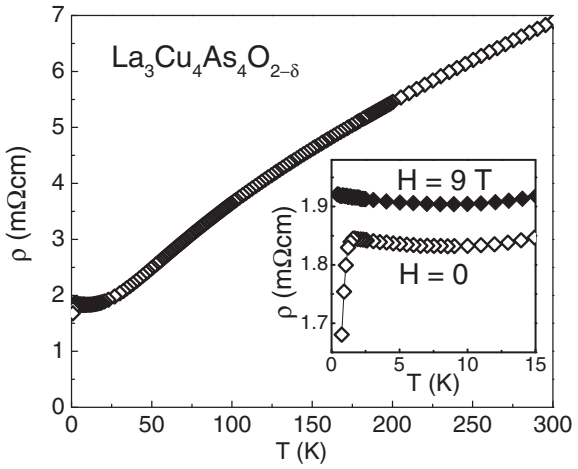

FIG. 7. The resistivity of $La_3Cu_4As_4O_{2-\delta}$ for $H = 0$. Inset: low-temperature resistivity of $La_3Cu_4As_4O_{2-\delta}$ showing a possible superconducting transition at around 1.3 K.

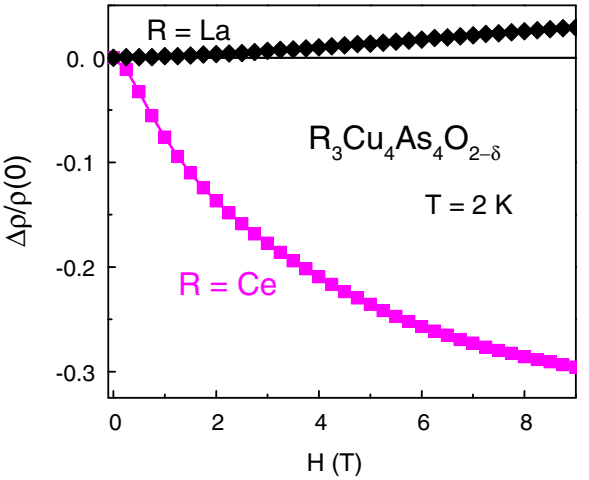

FIG. 8. (Color online) The magnetoresistance of $Ce_3Cu_4As_4O_{2-\delta}$ (squares) and $La_3Cu_4As_4O_{2-\delta}$ (diamonds) at 2 K from 0 to 9 T.

a maximum around the magnetic ordering temperature T_N, and to Fermi liquid behavior below T_N [30]. However, the heavy-fermion behavior in $Ce_3Cu_4As_4O_{2-\delta}$ is difficult to establish unequivocally from specific-heat measurements because of the magnetic transitions occurring between 1.9 and 24 K. Moreover, the complex field-dependent specific heat never results in a $\gamma T + \beta T^3$ dependence at low temperatures. The complex field dependence of the resistivity and specific heat of $Ce_3Cu_4As_4O_{2-\delta}$ are studied in detail elsewhere [26].

Notably, a significant reduction in the $Ce_3Cu_4As_4O_{2-\delta}$ resistivity is induced by magnetic field, as shown in Fig. 8. The corresponding magnetoresistance $\Delta\rho(H)/\rho(0) = [\rho(H) - \rho(0)]/\rho(0)$ reaches $\Delta\rho(9\text{ T})/\rho(0) \sim -0.33$. Such a value is comparable to that in the well-known giant magnetoresistance manganite compounds [31–33]. A possible reason for the large negative magnetoresistance is the formation of short-range magnetically ordered clusters, such as the Griffiths phase in manganites [34,35]. Such a scenario is consistent with the observation from neutron scattering measurements [26]. As expected for a paramagnetic metal, $La_3Cu_4As_4O_{2-\delta}$ shows small positive magnetoresistance at $T = 2$ K (diamonds, Fig. 8).

B. $Pr_3Cu_4As_4O_{2-\delta}$

Figure 9 shows the $Pr_3Cu_4As_4O_{2-\delta}$ inverse susceptibility H/M for $H = 0.1$ T, with the low-temperature M/H data presented in the inset. After subtracting a temperature-independent constant $M_0/H = 6.45 \times 10^{-4}$ emu/mol$_{Pr^{3+}}$, the magnetic susceptibility is well described by a Curie-Weiss law as $H/(M\text{-}M_0)$ becomes linear in T above ∼70 K. M_0 sums up the core diamagnetic and Pauli paramagnetic contributions. The effective moment determined from the linear fit of $H/(M\text{-}M_0)$ is $\mu_{\text{eff}} = 3.26\,\mu_B$, slightly smaller than the theoretical value $\mu_{\text{eff}}^{\text{th}} = 3.58\,\mu_B$ for Pr^{3+}. This discrepancy might be due to the presence of impurity phases, with XRD measurements showing a 90 wt % for the 3442 phase, with the rest consisting of PrCu and Pr_4As_3 secondary phases. The Weiss temperature θ_W, also obtained from the linear fit $\theta_W = 2.1$ K, and the

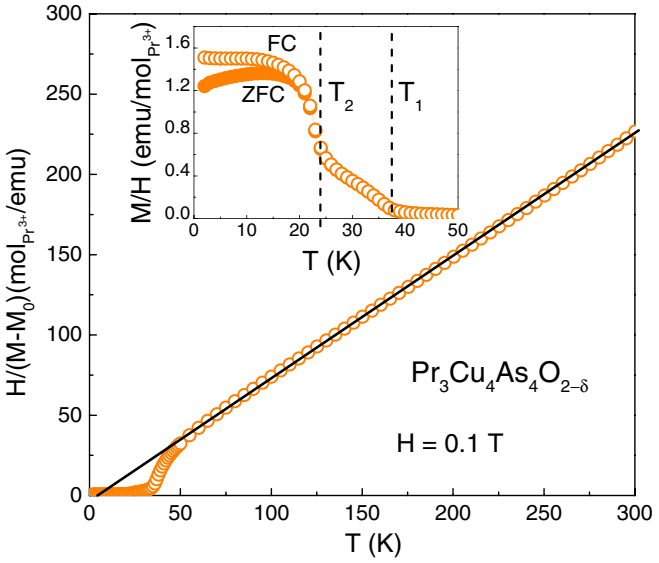

FIG. 9. (Color online) The temperature-dependent inverse susceptibility H/M of $Pr_3Cu_4As_4O_{2-\delta}$ for $H = 0.1$ T. The solid line is the extrapolated linear fit of H/M above 50 K. Inset: low-temperature ZFC (full symbols) and FC (open symbols). The transition temperatures T_1 and T_2 are marked by vertical dashed lines.

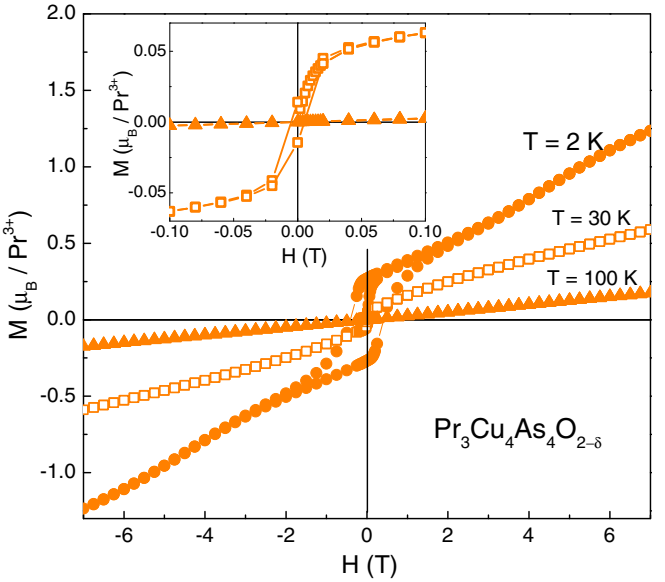

FIG. 10. (Color online) The magnetization isotherms of $Pr_3Cu_4As_4O_{2-\delta}$ at $T = 2$ K (circles), 30 K (squares), and 100 K (triangles). Inset: low-field magnetization isotherms at $T = 30$ and 100 K.

diverging $M(T)$ observed below $T_1 \sim 40$ K (inset, Fig. 9) are consistent with ferromagnetic coupling. However, no ZFC (full symbols) and FC (open symbols) irreversibility occurs until below a second transition temperature around $T_2 \sim 24$ K (inset, Fig. 9). The resulting T_1/θ_W ratio is unusually high, $T_1/\theta_W \geqslant 20$, a possible consequence of strong crystal electric field (CEF) and anisotropic coupling effects. By analogy with $Ce_3Cu_4As_4O_{2-\delta}$, the two transitions at T_1 and T_2 in the Pr compound might be attributed to short-range correlations. This short-range correlation might be attributed to a magnetic sublattice with 2D Ising-type correlations, as the Ising type of magnetic anisotropy is strongly favored by the local environment around the $R1$ site [22]. An alternate scenario could be that the ZFC-FC irreversibility that occurs only below T_2 is due to a cluster glass state occurring at low temperatures. Neutron scattering experiments are necessary to solve the magnetic structure in $Pr_3Cu_4As_4O_{2-\delta}$.

The magnetization isotherms of $Pr_3Cu_4As_4O_{2-\delta}$, shown in Fig. 10 for $T = 2$ K (circles), 30 K (squares), and 100 K (triangles), above and below the transitions at T_1 and T_2. The small magnetization values, less then 1.2 μ_B/Pr^{3+} at 7 T ($T = 2$ K), the nearly linear $M(H)$ isotherms, together with small hysteresis below T_1, favor the cluster glass scenario.

The specific heat of $Pr_3Cu_4As_4O_{2-\delta}$ (Fig. 11) displays two small peaks around T_1 and T_2, also indicating short-range correlations below T_1. An additional broad peak around 10 K in C_p may suggest a spin-glass state at low temperatures. However, the entropy associated with this latter peak may also be attributed to the paramagnetic impurities in the $Pr_3Cu_4As_4O_{2-\delta}$ sample. Given the difficulty in obtaining higher purity $Pr_3Cu_4As_4O_{2-\delta}$, neutron diffraction experiments are needed in order to identify the ground-state and anisotropy effects in this compound. By applying a field $H = 9$ T (not shown), the lower transition around 22 K is completely suppressed, while the upper one around 36 K remains unchanged.

The resistivity of $Pr_3Cu_4As_4O_{2-\delta}$ (Fig. 12) shows metallic behavior as it decreases nearly linearly down to $\sim T_1 = 40$ K. A drop in resistivity occurs at T_1, consistent with loss of spin-disorder scattering associated with ordering. The residual resistivity ratio is RRR ~ 16.5, indicative of good metallicity.

C. $La_3Ni_4As_4O_{2-\delta}$

Figure 13 shows the temperature-dependent susceptibility of $La_3Ni_4As_4O_{2-\delta}$ for $H = 0.1$ T, with the low-temperature $H = 5$ Oe data presented in the inset as $4\pi\chi$. Above 150 K, the

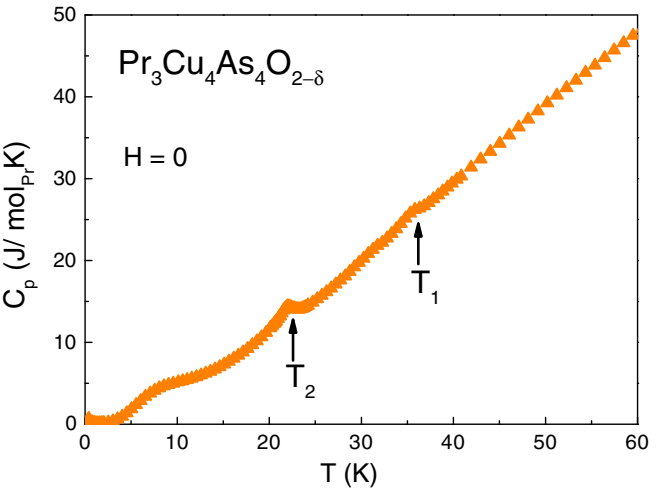

FIG. 11. (Color online) The specific heat of $Pr_3Cu_4As_4O_{2-\delta}$ for $H = 0$ with the transition temperatures T_1 and T_2 indicated by vertical arrows.

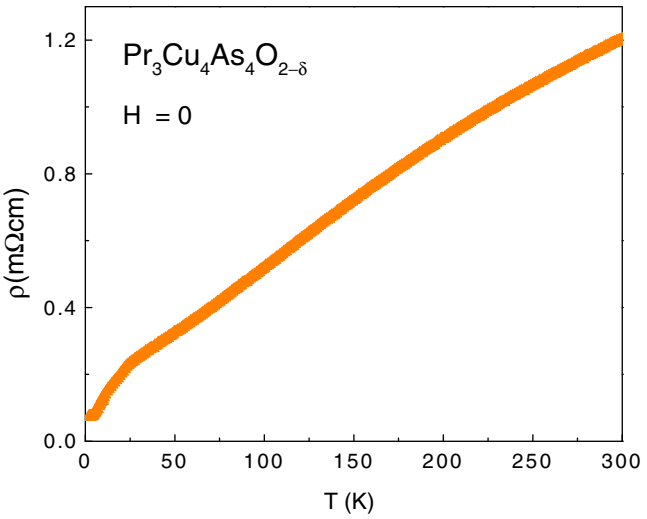

FIG. 12. (Color online) The resistivity of $Pr_3Cu_4As_4O_{2-\delta}$ for $H = 0$.

magnetization is almost temperature independent, as expected for a Pauli paramagnet. The low-temperature upturn in the $H = 0.1$ T magnetization could be due to impurities in the constituent elements. A Curie fit of the data below 50 K is consistent with ~0.03% Gd impurity. The $H = 0.1$ T magnetization indicates that Ni is Pauli paramagnetic in $La_3Ni_4As_4O_{2-\delta}$, similar to the cases for the Cu analogs discussed above.

When $H = 5$ Oe, the $4\pi\chi$ shown in the inset of Fig. 13 reveals superconductivity onset around 2 K, with a superconducting volume faction close to 14%. However, this might be an underestimate due to the instrumental temperature limit of 1.85 K, at which temperature $4\pi\chi$ is still diving down.

The specific heat of $La_3Ni_4As_4O_{2-\delta}$ in Fig. 14(a) confirms the bulk superconductivity for $H = 0$ (squares), while a field of $H = 1$ T (circles) pushes the transition below 0.4 K. A fit of the $H = 1$ T data to $C_p = \gamma T + \beta T^3 + A/T^2$ gives the electronic and phonon specific-heat coefficients $\gamma = 8.43\,\mathrm{mJ/mol_{La}K^2}$ and $\beta = 0.32\,\mathrm{mJ/mol_{La}K^4}$, respectively. The

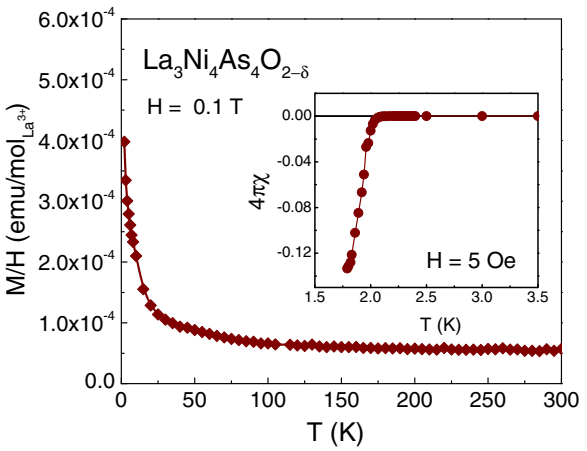

FIG. 13. (Color online) The magnetic susceptibility of $La_3Ni_4As_4O_{2-\delta}$ for $H = 0.1$ T. Inset: the low-field $4\pi\chi$ for $H = 5$ Oe.

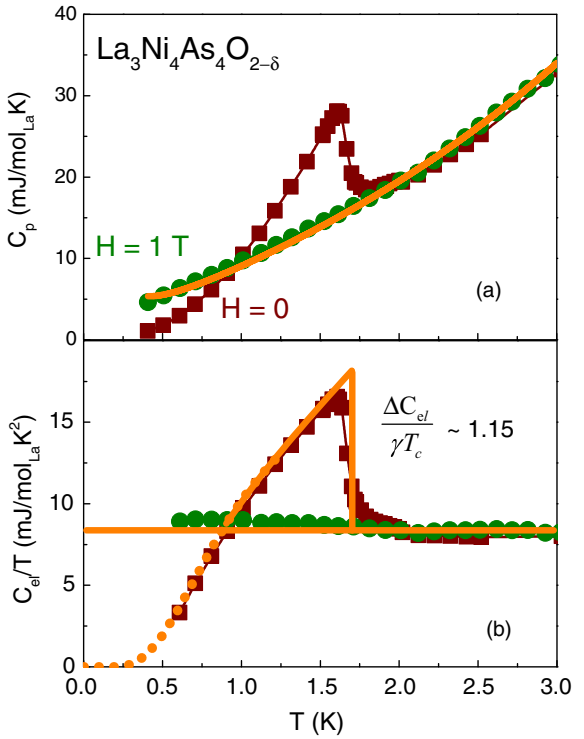

FIG. 14. (Color online) (a) The specific heat of $La_3Ni_4As_4O_{2-\delta}$ for $H = 0$ (squares) and 1 T (circles), with a $\gamma T + \beta T^2 + A/T^2$ fit (solid line) (see text). (b) The electronic specific-heat jump around the superconducting transition temperature, with the dotted line representing a BCS fit up to 1.3 K. The solid lines are used to estimate the electronic specific-heat jump at T_c.

A/T^2 represents a small nuclear Schottky contribution, with $A = 0.32\,\mathrm{mJK/mol_{La}}$. The electronic specific-heat coefficient is very close to the value of $8.29\,\mathrm{mJ/mol_{La}K^2}$ in the $La_3Ni_4P_4O_2$ superconductor [20].

Figure 14(b) shows the electronic specific-heat jump around the superconducting transition temperature for $La_3Ni_4As_4O_{2-\delta}$. The electronic specific heat is obtained as $C_{el} = C_p - \beta T^3 - A/T^2$, with β and A determined above. The jump in the electronic specific heat at transition temperature $T_C = 1.7$ K, $\Delta C_{el}/\gamma T_c$, is about 1.15, smaller but fairly close to the value of 1.44, expected for a weakly coupled BCS superconductor.

The $H = 0$ electronic specific heat can be fit by BCS theory up to 1.3 K. The dotted line in Fig. 14(b) represents the fit to $C_{el} = \mathrm{Ce}^{-\Delta(0)/k_BT}$, with $C = 107.55$ mJ/mol K and $\Delta(0) = 2.36$ K. The ratio $2\Delta(0)/k_BT_c \sim 2.77$ is indicative of a weakly coupled superconductor, to be confirmed with specific-heat measurement down to a much lower temperature region.

The temperature-dependent resistivity for $La_3Ni_4As_4O_{2-\delta}$ is shown in Fig. 15. A drop in the resistivity occurs close to 2 K for $H = 0$ (full symbols), consistent with the superconducting transition seen in the bulk measurements. However, the measured resistance values were close to the instrument sensitivity values, a possible explanation for the finite resistivity in the superconducting state. For $H = 0.8$ T (open symbols, inset in Fig. 15), the superconducting transition is suppressed below 0.4 K. Compared to the $La_3Cu_4As_4O_{2-\delta}$ compound, the

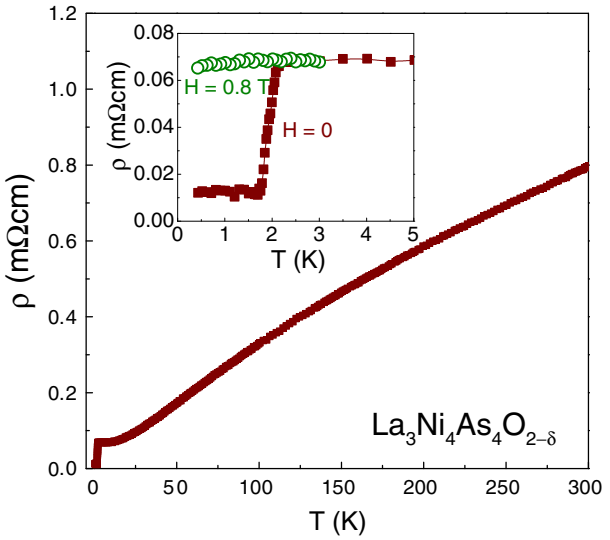

FIG. 15. (Color online) Temperature-dependent resistivity of $La_3Ni_4As_4O_{2-\delta}$ for $H = 0$. Inset: low-temperature resistivity for $H = 0$ (full symbols) and 0.8 T (open symbols).

resistivity values for $La_3Ni_4As_4O_{2-\delta}$ are about one order of magnitude smaller, and the residual resistivity ratio RRR = $\rho(300\ K)/\rho(3\ K)$ is 11.7, nearly three times larger than for the Cu analog. This might be explained by the fact that the Cu compound has a larger c lattice parameter, which significantly reduces the interlayer hopping.

D. $Ce_3Ni_4As_4O_{2-\delta}$

The temperature-dependent inverse magnetization $Ce_3Ni_4As_4O_{2-\delta}$ is shown in Fig. 16 for $H = 0.1$ T. In the temperature range between 2 and 300 K, no magnetic phase transition is observed. After subtracting a temperature-independent constant $M_0/H = 4.5 \times 10^{-4}$ emu/$mol_{Ce^{3+}}$, the magnetic susceptibility is well described by a Curie-Weiss law. The effective moment determined from the linear fit of $H/(M\text{-}M_0)$ is $\mu_{\rm eff} = 2.14\,\mu_B/Ce^{3+}$, slightly smaller than the theoretical value

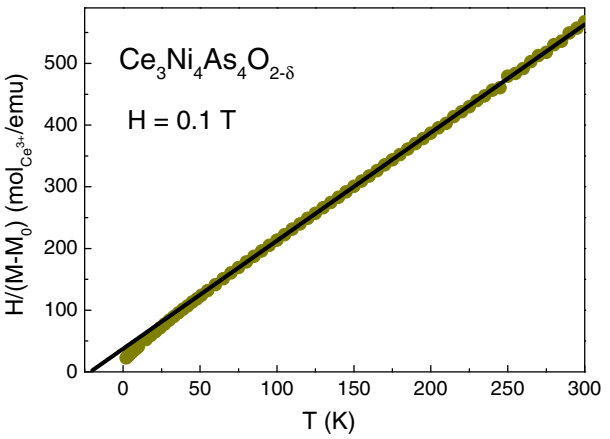

FIG. 16. (Color online) The temperature-dependent inverse susceptibility H/M of $Ce_3Ni_4As_4O_{2-\delta}$ for $H = 0.1$ T. The solid line is the extrapolated linear fit of H/M above 30 K.

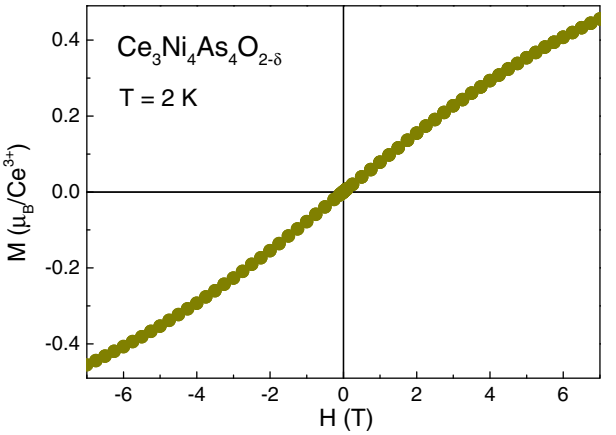

FIG. 17. (Color online) The magnetization isotherm of $Ce_3Ni_4As_4O_{2-\delta}$ at $T = 2$ K.

$\mu_{\rm eff}^{\rm th} = 2.54\ \mu_B/Ce^{3+}$. The likely implication is that Ce is in a 3+ state, where the constant magnetization term M_0 takes into account the contribution from conduction electron paramagnetism and core diamagnetism. The Weiss temperature θ_W, also obtained from the linear fit, is θ_W = –21 K, indicative of antiferromagnetic coupling between Ce^{3+} ions. With lack of phase transition down to 2 K, the negative Weiss temperature suggests possible frustration between Ce^{3+} magnetic moments, which needs to be further investigated.

The $T = 2$ K magnetization isotherm for $Ce_3Ni_4As_4O_{2-\delta}$ in Fig. 17 confirms the paramagnetic behavior seen in $M(T)$. At the maximum applied field $H = 7$ T, this compound is far from saturation, as the magnetization reaches 0.45 μ_B, much smaller than the saturated moment 2.14 μ_B for Ce^{3+}.

The resistivity measurement for $Ce_3Ni_4As_4O_{2-\delta}$ is shown in Fig. 18 for $H = 0$ (symbols, full) and 9 T (symbols, open). By contrast to its Cu analog, $Ce_3Ni_4As_4O_{2-\delta}$ shows metallic behavior for the whole measured temperature range, with a relatively small residual resistivity ratio RRR $\sim$ 2.4. The resistivity begins to drop steeply below 2 K, indicative of a possible phase transition. However, due to the temperature

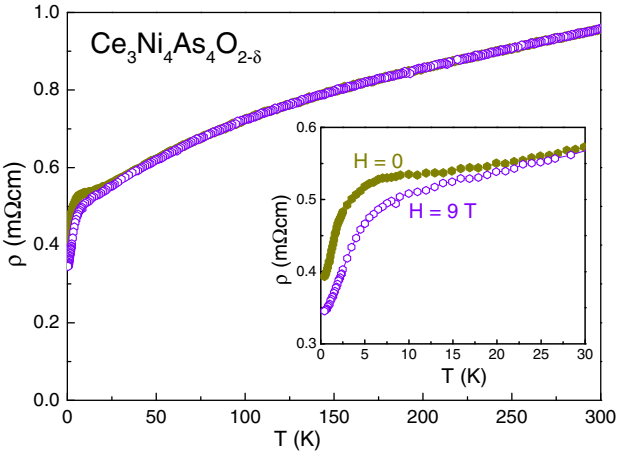

FIG. 18. (Color online) Temperature-dependent resistivity for $Ce_3Ni_4As_4O_{2-\delta}$ at $H = 0$ (full symbols) and 9 T (open symbols). Inset: enlarged view of the low-temperature resistivity.

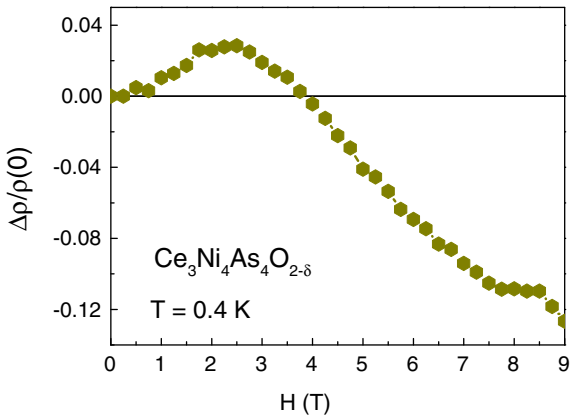

FIG. 19. (Color online) The $T = 0.4$ K magnetoresistance of $Ce_3Ni_4As_4O_{2-\delta}$.

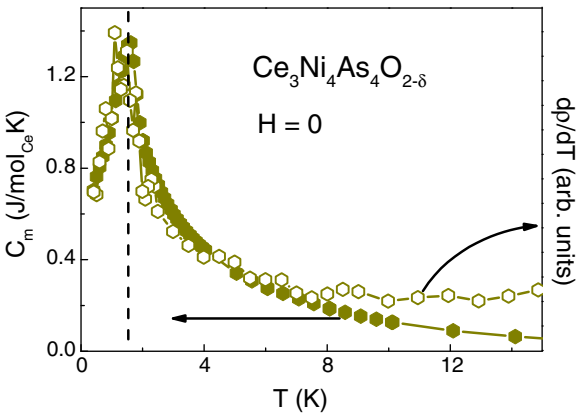

FIG. 21. (Color online) A combined plot of magnetic specific heat (left axis) and resistivity derivative (right axis) for $Ce_3Ni_4As_4O_{2-\delta}$.

range limit of our magnetization measurement, it is not clear whether this phase transition is associated with magnetic ordering or not. Below ~20 K, the $H = 9$ T resistivity values (open symbols, Fig. 18) are lower than for the $H = 0$ case.

The $T = 0.4$ K magnetoresistance for $Ce_3Ni_4As_4O_{2-\delta}$ in Fig. 19 confirms the low-temperature magnetoresistance. Compared with the Cu analog, $Ce_3Ni_4As_4O_{2-\delta}$ shows a relatively smaller magnetoresistance $\Delta\rho(H)/\rho(0) \sim -0.12$ at 9 T. Moreover, $\Delta\rho(H)/\rho(0)$ changes nonmonotonically with field. $\Delta\rho(H)/\rho(0)$ increases for $H < 2.5$ T, and then decreases as the field increases further to 9 T. Such a local maximum might be associated with a metamagnetic phase transition at 0.4 K since, as discussed in the following, this temperature appears to be lower than a possible magnetic ordering temperature at 1.7 K.

To confirm the phase transition indicated by the drop in resistivity at low temperatures, the specific-heat measurement for $Ce_3Ni_4As_4O_{2-\delta}$ is shown in Fig. 20. A sharp peak is indeed observed around 1.7 K. If we assume this phase transition to be due to magnetic ordering, the magnetic specific-heat contribution C_m can be calculated as $C_m(\text{Ce}) = C_p(\text{Ce})\text{-}C_p(\text{La})$, and is shown in Fig. 20 inset (symbols, left axis), together with the magnetic entropy S_m (line, right axis). Notably, the magnetic specific heat C_m remains finite up to temperatures an order of magnitude larger than the transition temperature. This suggests that short-range correlations might be present above the ordered state. Similar behavior has been reported in the Ising antiferromagnet $CeNi_2As_2$ [22], suggesting that the short-range correlations might be due to the coupling anisotropy in the 3442 or 122 layered compounds. The entropy at the ordering temperature is much smaller than R ln2, suggesting small moment ordering around 1.7 K.

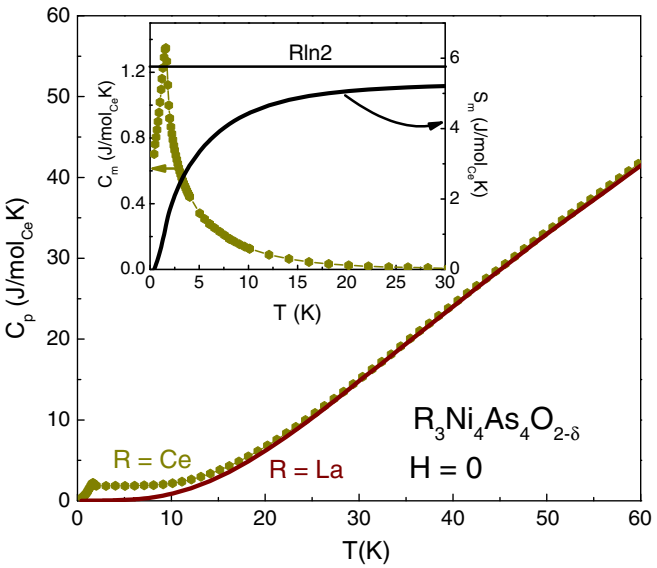

FIG. 20. (Color online) The specific heat of $R_3Ni_4As_4O_{2-\delta}$ for $R = $ Ce (symbols) and $R = $ La (solid line) for $H = 0$. Inset: magnetic specific heat (symbols, left axis) and entropy (solid line, right axis) of $Ce_3Ni_4As_4O_{2-\delta}$.

A combined plot of the magnetic specific heat C_m (left, full symbols) and the resistivity derivative $d\rho/dT$ (right, open symbols) for $Ce_3Ni_4As_4O_{2-\delta}$ is shown in Fig. 21. It can be seen that the magnetic specific heat and the resistivity derivative show matching peaks around the phase transition temperature at 1.7 K, as expected for an antiferromagnetically ordered metal [36].

E. $Pr_3Ni_4As_4O_{2-\delta}$

Figure 22 shows the $Pr_3Ni_4As_4O_{2-\delta}$ inverse susceptibility $H/(M-M_0)$ for $H = 5$ Oe, after the temperature-independent part $M_0/H = 3 \times 10^{-4}$ emu/mol$_{Pr^{3+}}$ was accounted for. The inset shows the ZFC (full symbols) and FC (open symbols) low temperature M/H. The irreversibility of the low temperature M/H, steep increase of the magnetization below the ordering temperature, and the saturation of the FC magnetization at low temperatures suggest ferromagnetic ordering in this compound. At high temperatures, the magnetic susceptibility is well described by a Curie-Weiss law as $H/(M\text{-}M_0)$ becomes linear in T above ~70 K. The effective moment determined from the linear fit of $H/(M\text{-}M_0)$ is $\mu_{\text{eff}} = 3.18\,\mu_B/Pr^{3+}$, slightly smaller than the theoretical value $\mu_{\text{eff}}^{\text{th}} = 3.58\,\mu_B/Pr^{3+}$, indicating that the Pr ion is in a 3+ state. This discrepancy is possibly due to the small amounts of secondary phases, as mentioned earlier. The Weiss temperature θ_W determined from the fit is $\theta_W \sim -7$ K, suggesting possible antiferromagnetic

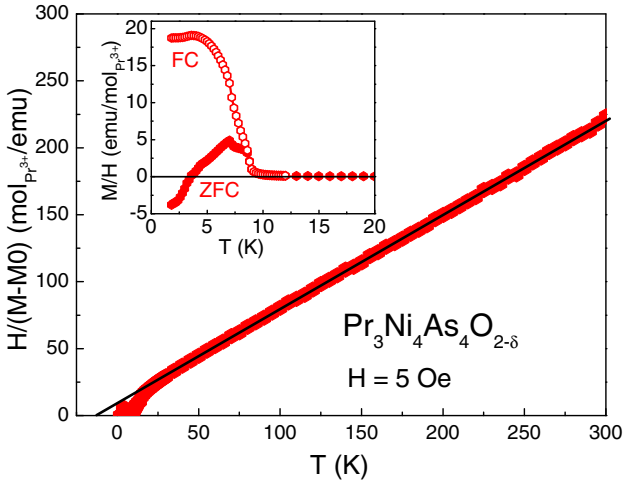

FIG. 22. (Color online) The temperature-dependent inverse susceptibility $H/(M\text{-}M_0)$ of $Pr_3Ni_4As_4O_{2-\delta}$ for $H = 5$ Oe. The solid line is the extrapolated linear fit of H/M above 30 K. Inset: ZFC (full) and FC (open) temperature-dependent M/H of $Pr_3Ni_4As_4O_{2-\delta}$.

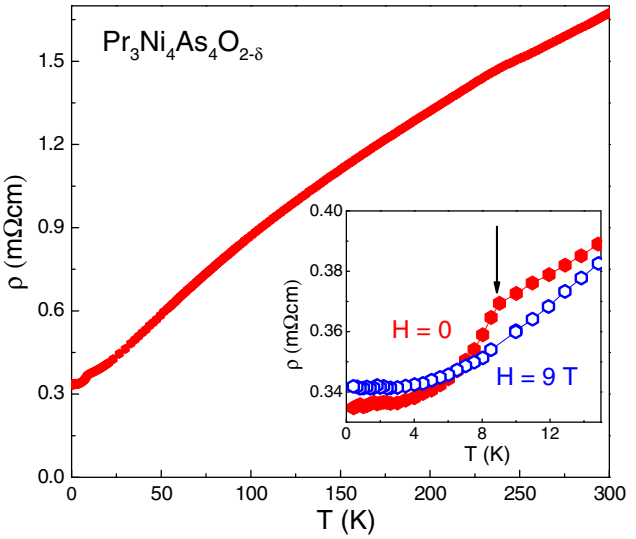

FIG. 24. (Color online) Temperature-dependent resistivity for $Pr_3Ni_4As_4O_{2-\delta}$ at $H = 0$. Inset: resistivity of $Pr_3Ni_4As_4O_{2-\delta}$ for $H = 0$ (full) and 9 T (open symbols).

coupling. However, the shape of the susceptibility and ZFC-FC irreversibility below the magnetic ordering temperature are typical of ferromagnetic order. Thus, a plausible explanation for the magnetic ground state would rely on strong crystal-field effects and highly anisotropic coupling. Neutron diffraction experiments are necessary to understand the detailed magnetic structure in this compound.

The magnetization isotherms for $Pr_3Ni_4As_4O_{2-\delta}$, shown in Fig. 23 for $T = 2$ (full) and 60 K (open), are similar to the corresponding data for the Cu analog. While the hysteresis in the $T = 2$ K curve is consistent with the ZFC-FC irreversibility in the $M(T)$ data, the coercive field $H_c = 0.05$ T is an order

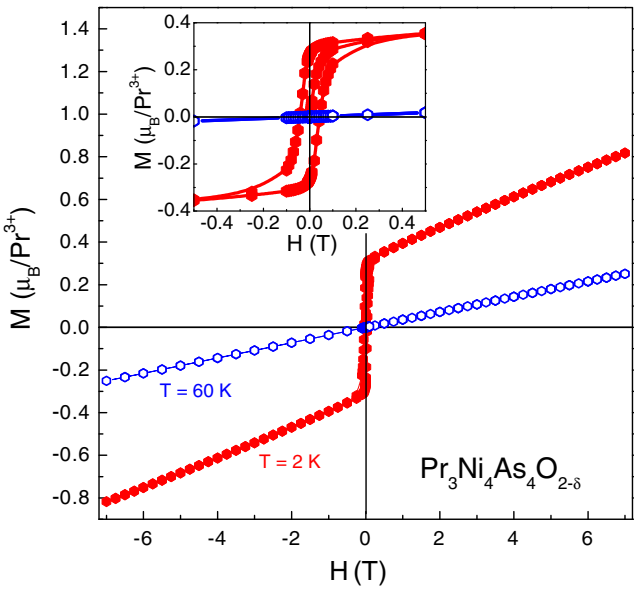

FIG. 23. (Color online) The magnetization isotherms of $Pr_3Ni_4As_4O_{2-\delta}$, measured at $T = 2$ (full symbols) and 60 K (open symbols). Inset: detailed view of the low-field magnetization isotherms.

of magnitude smaller than that of $Pr_3Cu_4As_4O_{2-\delta}$ (0.4 T). After the initial abrupt increase in the 2 K $M(H)$, a linear field dependence is registered up to 7 T, while the 60-K isotherm is linear through the whole measured field range. This results in a small remanent magnetization $M_r = 0.3\,\mu_B/Pr^{3+}$ at $T = 2$ K, close to the value for the analog's Cu compound. Notably, the moment at 7 T is much smaller than the theoretical saturated moment $\mu_{sat} = 3.2\,\mu_B$, due to either crystal-field effects or interaction anisotropy, or both.

Just like the magnetization data of $Pr_3Ni_4As_4O_{2-\delta}$, the resistivity is also similar with the Cu analog, as shown in Fig. 24. $Pr_3Ni_4As_4O_{2-\delta}$ displays metallic behavior down to 0.4 K, with the residual resistivity ratio RRR ~ 5. A resistivity drop is observed around 9 K in $H = 0$ data (full symbols, inset of Fig. 24), likely associated with the loss of spin-disorder scattering at the magnetic ordering. For $H = 9$ T (open symbols, inset of Fig 24), the transition is suppressed below the minimum measured temperature.

The specific heat of $Pr_3Ni_4As_4O_{2-\delta}$ is shown in Fig. 25. A sharp peak around 7.5 K in $H = 0$ data (full symbols, Fig. 25) is consistent with the magnetic ordering observed in magnetization and resistivity measurement (Figs. 22 and 24, respectively). This peak is suppressed below 0.4 K by a 9-T field (open symbols). At the lowest measured temperatures, an upturn in C_p could be attributed to another lower-temperature transition, or to a nuclear Schottky anomaly.

Doping experiments on $Pr_3Ni_4As_4O_{2-\delta}$ revealed preferential substitution on the two Pr crystallographic sites. $Pr_{3-x}La_xNi_4As_4O_{2-\delta}$ samples have been synthesized for $x = 1$ and 2. The inverse susceptibility $H/(M\text{-}M_0)$ of the $Pr_{3-x}La_xNi_4As_4O_{2-\delta}$ compounds are shown in Fig. 26 for $x = 0$ (circles), $x = 1$ (stars), and $x = 2$ (triangles), together with the magnetization M/H at low temperature in the inset. As the La content increases, the Curie temperature T_C gradually decreases from 8 ($x = 0$) to 3 K ($x = 2$), as expected for such a dilution of the magnetic ions. The effective moment for the $x = 1$ compound is $3.26\,\mu_B$, close to that of

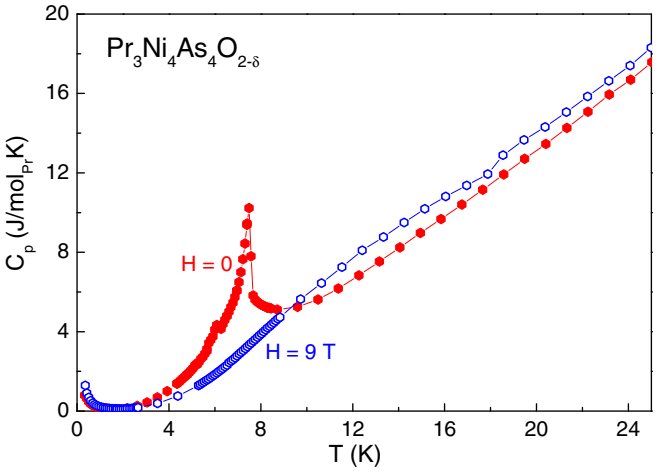

FIG. 25. (Color online) Temperature-dependent specific heat of $Pr_3Ni_4As_4O_{2-\delta}$ for $H = 0$ (full) and 9 T (open symbols).

the pure Pr compound, while it was significantly lower $\mu_{\rm eff} = 2.81\,\mu_B$ for $x = 2$. Both doped compounds show negative Weiss temperatures -10.7 K for $x = 1$ and -13.5 K for $x = 2$.

Field-dependent magnetization data for $Pr_{3-x}La_xNi_4As_4O_{2-\delta}$ are shown in Fig. 27. The coercive field gradually decreases as the La content increases (inset, Fig. 27). The remanent magnetization shows little change with the La doping.

From the XRD refinement on $Pr_{3-x}La_xNi_4As_4O_{2-\delta}$ samples, the doped La preferentially occupies the $R1$ rare-earth sites. In both $x = 1$ and 2 cases, the interlayer coupling for Pr ions is weakened compared with the $Pr_3Ni_4As_4O_{2-\delta}$ case. In the $x = 2$ case, the intralayer coupling is also weaker since the average distance between Pr layers has now doubled. It is thus reasonable that the Curie temperature decreases with the increase of La doping.

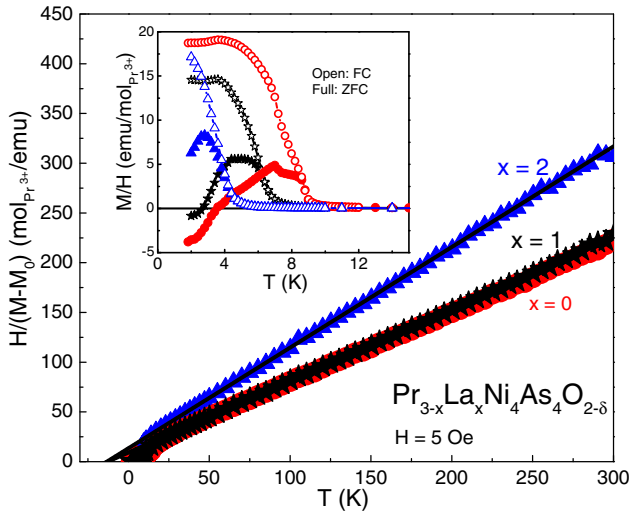

FIG. 26. (Color online) Temperature-dependent inverse susceptibility of $Pr_{3-x}La_xNi_4As_4O_{2-\delta}$ ($x = 0$, 1, and 2) (symbols). The solid lines are the extrapolated linear fits of $H/(M\text{-}M_0)$ above 30 K. Inset: ZFC (full) and FC (open) temperature-dependent susceptibility of $Pr_{3-x}La_xNi_4As_4O_{2-\delta}$ ($x = 0$, 1, and 2).

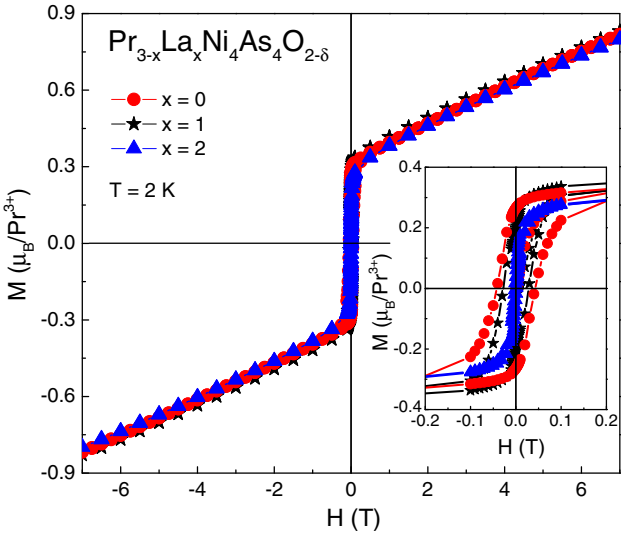

FIG. 27. (Color online) The hysteresis loop of $Pr_{3-x}La_xNi_4As_4O_{2-\delta}$ ($x = 0$, 1, and 2). Inset: a zoomed-in view of the low-field data.

F. $Nd_3Ni_4As_4O_{2-\delta}$

Figure 28 shows the $Nd_3Ni_4As_4O_{2-\delta}$ inverse susceptibility H/M for $H = 5$ Oe, with the low-temperature M/H data in the inset. The linear H/M above 25 K indicates Curie-Weiss behavior. The linear fit of H/M gives an effective moment $\mu_{\rm eff} = 3.55\,\mu_B$, close to the theoretical value $\mu_{\rm eff}^{\rm th} = 3.62\,\mu_B$ for Nd^{3+}. A negative Weiss temperature $\theta_W =$ –17.9 K indicates antiferromagnetic coupling. However, the ZFC-FC susceptibility (inset, Fig. 28) shows irreversibility below 7 K, which is usually attributed to ferromagnetic order or freezing of a spin-disordered state. The negative Weiss

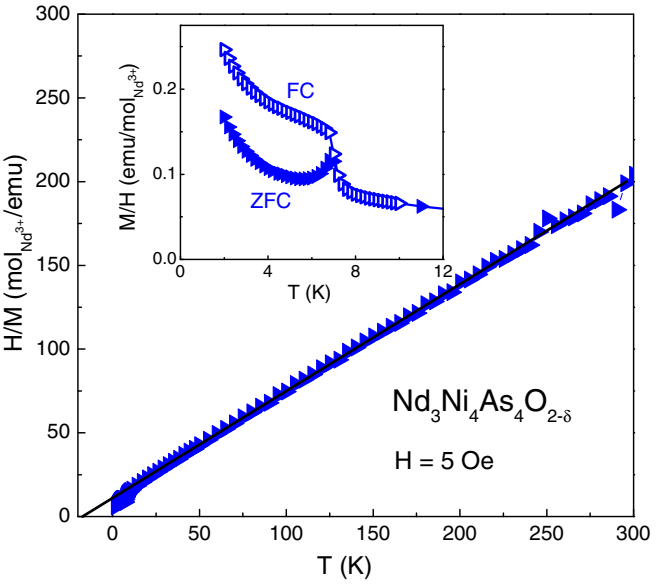

FIG. 28. (Color online) The inverse susceptibility H/M of $Nd_3Ni_4As_4O_{2-\delta}$ (blue symbols). The solid line is the extrapolated linear fit of H/M above 30 K. Inset: ZFC and FC magnetizations show an irreversibility below 7 K.

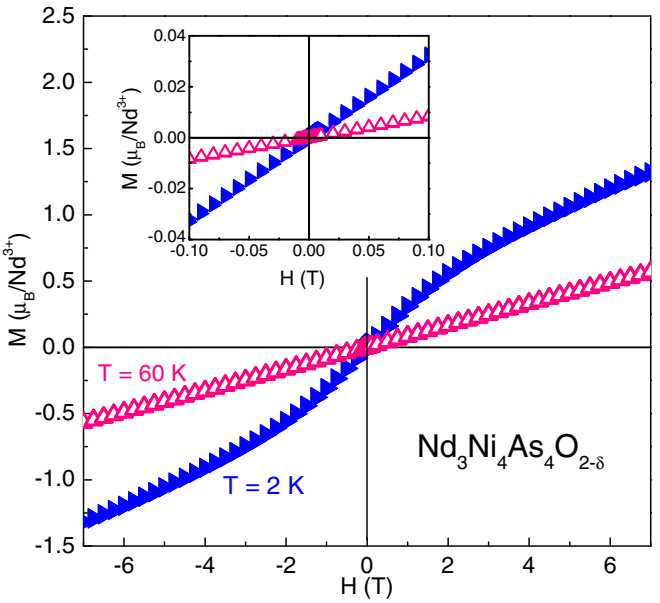

FIG. 29. (Color online) The magnetization isotherms for $Nd_3Ni_4As_4O_{2-\delta}$, measured at $T = 2$ (full symbols) and 60 K (open symbols). Inset: an enlarged view of the low-field data.

temperature is consistent with the latter scenario, i.e., frustrated antiferromagnetic coupling resulting in spin-glass behavior. This is also reenforced by the field-dependent magnetization measurements (Fig. 29) since no hysteresis is observed in the slowly increasing $M(H)$ isotherms, both below and above the irreversibility temperature.

In order to verify the spin-glass behavior in $Nd_3Ni_4As_4O_{2-\delta}$, ac magnetization measurements were performed, using ac field with amplitude $H_{ac} = 10$ Oe and frequency up to 10 kHz. As seen in Fig. 30, the peak around 7 K observed in the dc susceptibility moves up in temperature

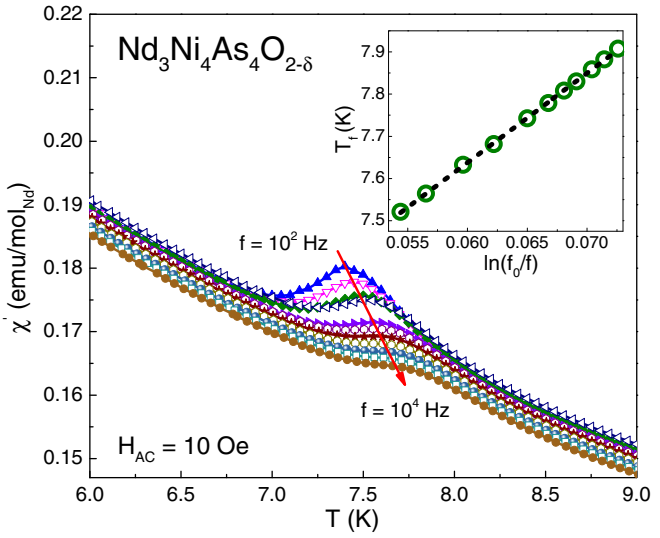

FIG. 30. (Color online) The frequency-dependent real part of the ac susceptibility χ' of $Nd_3Ni_4As_4O_{2-\delta}$. Inset: semilog plot of T_f vs $\ln(f_0/f)$, with T_f determined as maximal in χ'. The dotted line is a fit to the formula $f = f_0(T_f/T_0 - 1)^{z\nu}$.

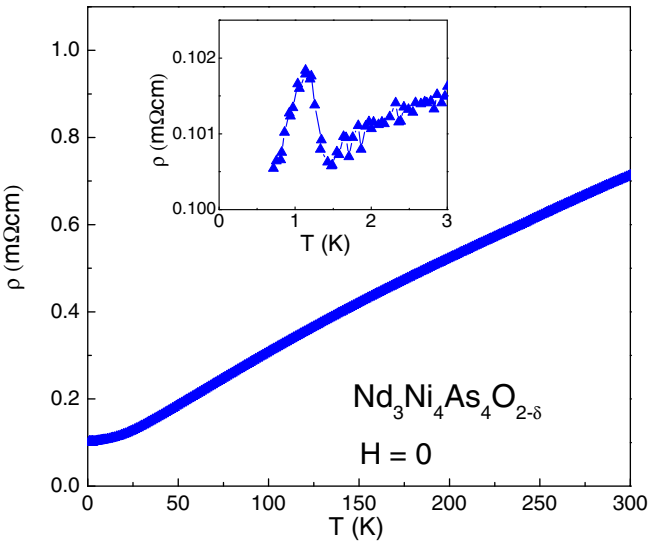

FIG. 31. (Color online) Temperature-dependent resistivity of $Nd_3Ni_4As_4O_{2-\delta}$ for $H = 0$. Inset: detailed view of the low-temperature resistivity.

with increasing frequency f in the ac data. By fitting the peak with a pseudo-Voigt function [37] on top of a Curie-Weiss background, the freezing temperature T_f is determined as a function of f. For a spin glass, this is expected to follow an exponential behavior [38]

$$f = f_0(T_f/T_0 - 1)^{z\nu}, \quad (1)$$

where f_0 represents characteristic frequency of a spin-glass system and T_0 is the dc limit of the freezing temperature.

The inset in Fig. 30 displays a semilog plot of T_f versus $1/(\ln f)$ (symbols), together with the linear fit according to Eq. (1), which gives $f_0 = 9.6 \times 10^9$ Hz, $T_0 = 7.21$ K, and $z\nu = 5.9$. The exponent $z\nu$ lies well within the 2–12 range for typical spin-glass systems [38,39]. The characteristic frequency f_0 is closer to a typical single atomic spin-glass system with $f_0 \approx 10^{12}$ Hz than a cluster glass system $f_0 \approx 10^4$ Hz [39,40]. This observation implies Nd^{3+} ions, instead of magnetic domains or clusters, to be responsible for spin-glass behavior.

A possible reason for the spin-glass state in $Nd_3Ni_4As_4O_{2-\delta}$ is site disorder, combined with interaction anisotropy. Site disorder is inferred from XRD refinement which indicates 22.5% oxygen deficiency. This results in disorder in the $(R2)_2O_2$ layer [Fig. 1(a)], while the interaction anisotropy could be expected by analogy with $Ce_3Cu_4As_4O_{2-\delta}$ [26].

The $Nd_3Ni_4As_4O_{2-\delta}$ shows metallic behavior for most of the measured temperature range, while a surprising sharp peak is present below 1.5 K (inset, Fig. 31). An increase in $\rho(T)$ on cooling would, in general, be associated with some Fermi surface instability (charge density wave), but the very low temperature and the sharpness of the peak suggest a first-order phase transition. Remarkably, a peak at the same temperature is revealed by the $H = 0$ specific heat (full symbols, Fig. 32), while a 9-T field (open symbols, Fig. 32) suppresses the associated transition as a broad Schottky peak moves closer to 4 K. The origin of the 1-K transition seen in both resistivity and specific heat remains to be investigated with field-dependent

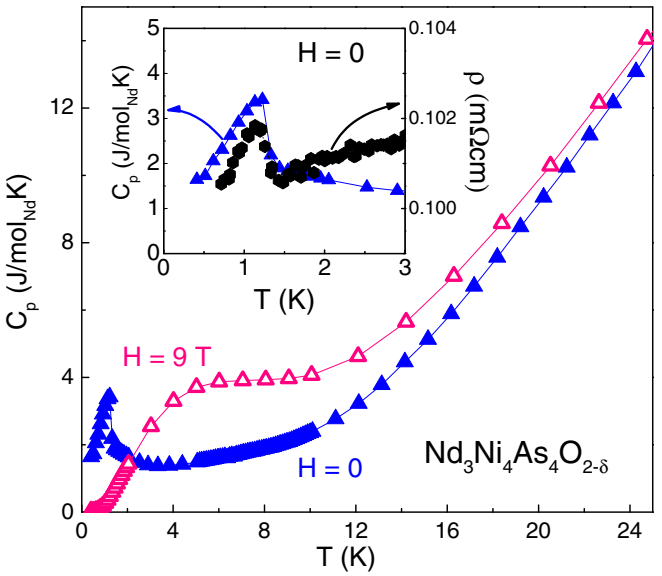

FIG. 32. (Color online) Temperature-dependent specific heat of $Nd_3Ni_4As_4O_{2-\delta}$, measured at $H = 0$ (full) and 9 T (open symbols). Inset: detailed view of the low-temperature specific heat (triangles) together with the resistivity (hexagons).

measurements, as well as neutron diffraction experiments. The lack of any phase transition signatures around 7 K in the specific heat of $Nd_3Ni_4As_4O_{2-\delta}$ (Fig. 32) is consistent with the spin-glass scenario in this compound.

G. $Sm_3Ni_4As_4O_{2-\delta}$

The temperature-dependent inverse susceptibility $H/(M\text{-}M_0)$ of $Sm_3Ni_4As_4O_{2-\delta}$ for $H = 0.1$ T is shown in Fig. 33, with the low temperature M/H displayed in the inset. After a temperature-independent value $M_0/H = 9.5 \times 10^{-4}$ emu/mol$_{Sm^{3+}}$ was subtracted, Curie-Weiss behavior is

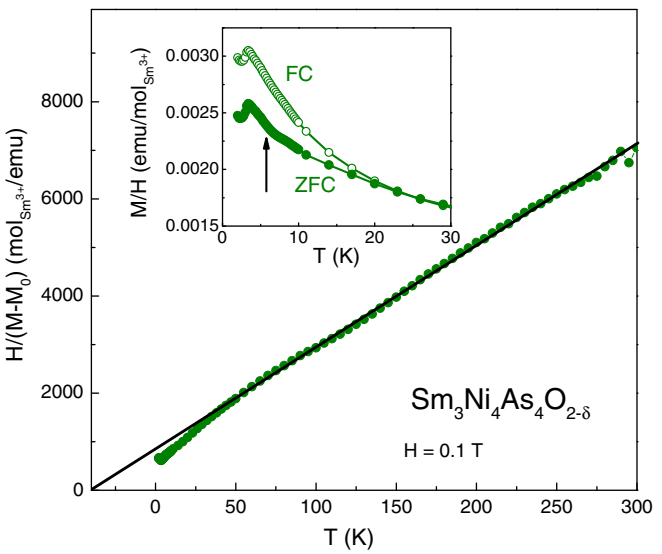

FIG. 33. (Color online) The temperature-dependent inverse susceptibility $H/(M\text{-}M_0)$ of $Sm_3Ni_4As_4O_{2-\delta}$ for $H = 0.1$ T. The solid line is the extrapolated linear fit of H/M above 50 K. Inset: detailed view of the low-temperature ZFC (full) and FC (open) susceptibility.

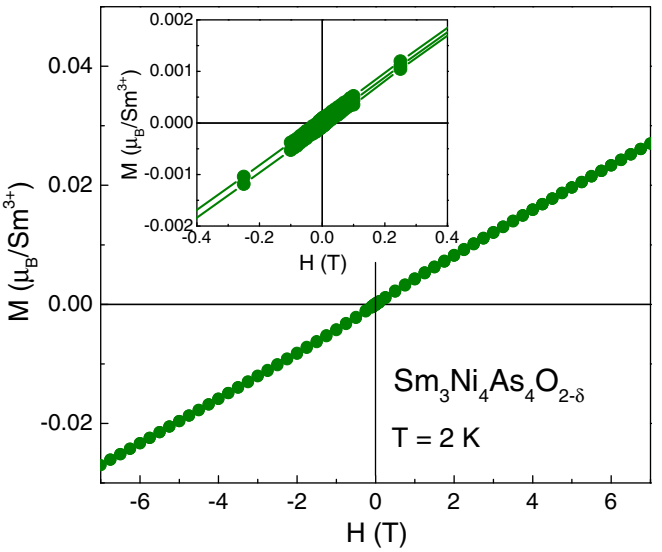

FIG. 34. (Color online) The magnetization isotherms for $Sm_3Ni_4As_4O_{2-\delta}$ measured at $T = 2$ K. Inset: detailed view of the low-field magnetization isotherms data.

observed above 50 K as $H/(M\text{-}M_0)$ is linear in temperature up to 300 K. From the linear fit of $H/(M\text{-}M_0)$ above 50 K, a negative Weiss temperature $\theta_W = -40.4$ K is determined. The effective moment $\mu_{\rm eff} = 0.62\,\mu_B$ is smaller than the theoretical value $\mu_{\rm eff}^{\rm th} = 0.85\,\mu_B/{\rm Sm}^{3+}$. The relatively large difference between the experimental and calculated effective moments is likely due to crystal-field effects typical for Sm compounds [41,42]. Similar behavior was reported, for example, in $SmNi_2B_2C$ [43]. At low temperatures, the magnetic susceptibility for $Sm_3Ni_4As_4O_{2-\delta}$ reveals magnetic ordering below ~3.5 K (inset, Fig. 33), as a cusp is present in M/H.

The cusp around 3.5 K in Fig. 33 signals an antiferromagnetic phase transition, consistent with the negative Weiss temperature. The fact that the actual phase transition temperature is much smaller than the Weiss temperature, i.e., $|\theta_W|/T_N > 11.5$, is suggestive of magnetic frustration of the Sm^{3+} moments. This magnetic frustration may explain the

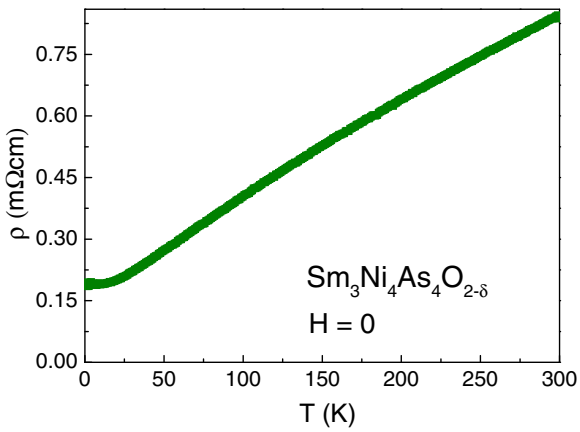

FIG. 35. (Color online) Temperature-dependent resistivity of $Sm_3Ni_4As_4O_{2-\delta}$ for $H = 0$.

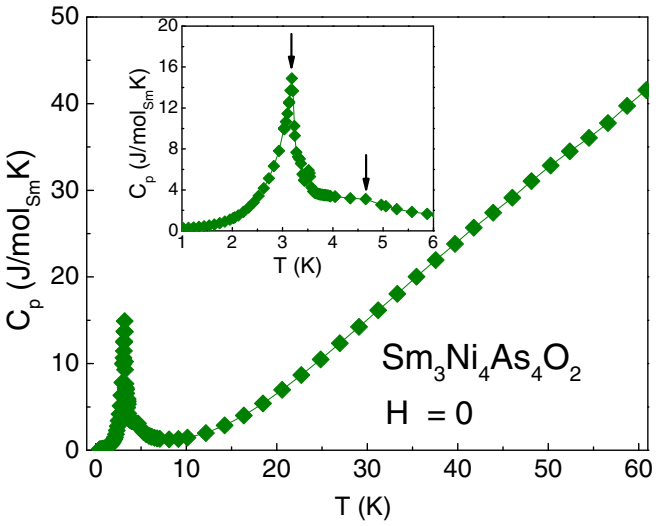

FIG. 36. (Color online) The specific heat of $Sm_3Ni_4As_4O_{2-\delta}$ for $H = 0$. Inset: detailed view of the low-temperature specific heat, with vertical arrows marking the magnetic transitions.

ZFC-FC $M(T)$ irreversibility (inset, Fig. 33) occurring below 20 K, significantly higher than the ordering temperature at 3.5 K. Such irreversibility is usually related to short-range correlation above the ordering temperature.

The $T = 2$ K magnetization isotherm of $Sm_3Ni_4As_4O_{2-\delta}$ is shown in Fig. 34. Consistent with the irreversibility seen in $M(T)$ (Fig. 33), $M(H)$ displays small but finite hysteresis. This could also be a consequence of short-range correlations as indicated by the $M(T)$ measurement. Notably, the moment at 7 T is 0.03 μ_B/Sm^{3+}, much smaller than the Hund's rule saturated moment $\mu_{sat} = 0.71\ \mu_B/Sm^{3+}$.

The resistivity of $Sm_3Ni_4As_4O_{2-\delta}$ for $H = 0$ is shown in Fig. 35. Metallic behavior is observed for the temperature range from 2 to 300 K. The residual resistivity ratio is RRR $\sim$ 4.4, comparable to that of other $R_3Ni_4As_4O_{2-\delta}$ compounds.

Even though not visible in the resistivity, the phase transition observed in magnetization is confirmed by the specific heat of $Sm_3Ni_4As_4O_{2-\delta}$ shown in Fig. 36. A sharp peak at 3.0 K is consistent with the cusp in magnetization shown in Fig. 33. A much smaller peak around 4.6 K appears around the same temperature where an inflection point is noticeable in the ZFC M/H data (arrow, inset Fig. 33). This might be associated with the short-range order in this compound, or with a small amount of impurity, or both.

IV. CONCLUSIONS

Given their crystal structure, poor metallicity, and complex magnetic behavior, the $R_3T_4As_4O_{2-\delta}$ compounds are closely related to the superconducting Fe-pnictides. However, the transition metal T for which the 3442 phase is stabilized differs from Fe, and no high-temperature superconductivity occurs. Instead, changing the rare earth R and transition metal T in $R_3T_4As_4O_{2-\delta}$ compounds results in varied magnetic and transport properties. For T = Cu, the compounds with R = La–Pr display larger interlayer spacing than the Ni compounds, resulting in reduced interlayer hopping and conductivity. This is confirmed by the fact that the Ni compounds show resistivity values typically an order of magnitude smaller than their Cu analogs. As expected, the R = La compounds in both T = Cu, Ni series show Pauli paramagnetic behavior. $La_3Ni_4As_4O_{2-\delta}$ becomes superconducting below $T_c = 1.7$ K, with a specific-heat jump $\Delta C_{el}/\gamma T_c$ (Fig. 14) close to but slightly smaller than the predicted BCS value. This compound is therefore very similar to its P analog $La_3Ni_4P_4O_2$ [20]. Despite a superconducting signal in $\rho(T)$ for the Cu analog around 1 K, bulk superconductivity can not be unambiguously confirmed in $La_3Cu_4As_4O_{2-\delta}$.

$Ce_3Cu_4As_4O_{2-\delta}$ stands out among all compounds presented here, the only nonmetal, with complex field dependence of the magnetization, specific heat, and resistivity (Figs. 3, 5, and 6). This compound shows up to three possible transitions in both magnetization and specific heat, although the peak in C_p (Fig. 5) is small for the upper transition, and becomes increasingly larger for the lower transitions. Preliminary neutron experiments [26] suggest short-range order, or partial order on the two different Ce sites, above $\sim$2 K, with long-range order below the $T = 1.9$ K transition. Large negative magnetoresistance $\Delta\rho/\rho_0 = -30\%$ is also observed at low temperatures in $Ce_3Cu_4As_4O_{2-\delta}$ (Fig. 8), while the Ni analog has a smaller, albeit still significant, negative magnetoresistance close to -12% (Fig. 19). All other compounds reported here show only negligible magnetoresistance (not shown). A detailed study of the field dependence of the specific heat and resistivity in $Ce_3Cu_4As_4O_{2-\delta}$ reveals non-Fermi liquid and potential heavy-fermion behavior in this compound [26].

$Pr_3Cu_4As_4O_{2-\delta}$ shows ferromagnetic order below 40 K (Fig. 9). No other $R_3T_4As_4O_{2-\delta}$ with heavier rare earths have been stabilized so far. Similar to the 1111 series, pressure might be required to synthesize additional 3442 members of the Cu series.

When T = Ni, the Ce compound shows a possible antiferromagnetic phase transition around 1.7 K (Figs. 18 and 20). Upon changing the rare earth from R = Pr to Nd to Sm, the magnetic ground state of $R_3Ni_4As_4O_{2-\delta}$ varies from ferromagnetism to spin glass to antiferromagnetism, respectively.

In conclusion, two series of $R_3T_4As_4O_{2-\delta}$ compounds (T = Cu and Ni) have been investigated with crystallographic, thermodynamic, and transport property measurements. Their crystal structure represents a convolution of the 122 and 1111 Fe pnictide structures, making them potential candidates for high-temperature superconductivity. Only the nonmagnetic member R = La and T = Ni shows superconductivity below 1.7 K. While it may also occur for the R = La and T = Cu compounds, the superconducting transition seen in $\rho(T)$ is not yet confirmed by other measurements. Lack of the superconductivity for the rest of the series points to the importance of the d^6 electron configuration. Ongoing experiments are aimed at synthesizing additional 3442 compounds, with Fe and other transition metals. Further investigation of the newly discovered superconductor $La_3Ni_4As_4O_{2-\delta}$ includes pressure and doping studies, while the field-dependent properties of $Ce_3Cu_4As_4O_{2-\delta}$ are being investigated with neutron scattering experiments.

ACKNOWLEDGMENTS

The work at Rice University was supported by AFOSR MURI. We also acknowledge the Office of the Assistant Secretary of Defense for Research and Engineering for providing the funds that supported part of this research (H.H. and M.C.A.). The authors thank P. Dai, L. Zhao, and S. Zhou for useful discussions.

[1] Y. Kamihara, T. Watanabe, M. Hirano, and H. Hosono, J. Am. Chem. Soc. **130**, 3296 (2008).
[2] Marianne Rotter, Marcus Tegel, and Dirk Johrendt, Phys. Rev. Lett. **101**, 107006 (2008).
[3] Patricia L. Alireza, Y. T. Chris Ko, Jack Gillett, Chiara M. Petrone, Jacqueline M. Cole, Gilbert G. Lonzarich, and Suchitra E. Sebastian, J. Phys.: Condens. Matter **21**, 012208 (2009).
[4] Hiroki Takahashi, Kazumi Igawa, Kazunobu Arii, Yoichi Kamihara, Masahiro Hirano, and Hideo Hosono, Nature (London) **453**, 376 (2008).
[5] Chien-Lung Huang, Chih-Chieh Chou, Kuo-Feng Tseng, Yi-Lin Huang, Fong-Chi Hsu, Kuo-Wei Yeh, Mau-Kuen Wu, and Hung-Duen Yang, J. Phys. Soc. Jpn. **78**, 084710 (2009).
[6] Hisashi Kotegawa, Yuuki Tao, Hideki Tou, Hiraku Ogino, Sigeru Horii, Kohji Kishio, and Jun-ichi Shimoyama, J. Phys. Soc. Jpn. **80**, 014712 (2011).
[7] S. Nandi, M. G. Kim, A. Kreyssig, R. M. Fernandes, D. K. Pratt, A. Thaler, N. Ni, S. L. Bud'ko, P. C. Canfield, J. Schmalian, R. J. McQueeney, and A. I. Goldman, Phys. Rev. Lett. **104**, 057006 (2010).
[8] G. F. Chen, Z. Li, D. Wu, G. Li, W. Z. Hu, J. Dong, P. Zheng, J. L. Luo, and N. L. Wang, Phys. Rev. Lett. **100**, 247002 (2008).
[9] M. M. Qazilbash, J. J. Hamlin, R. E. Baumbach, Lijun Zhang, D. J. Singh, M. B. Maple, and D. N. Basov, Nat. Phys. **5**, 647 (2009).
[10] Qimiao Si and Elihu Abrahams, Phys. Rev. Lett. **101**, 076401 (2008).
[11] Satoru Matsuishi, Yasunori Inoue, Takatoshi Nomura, Hiroshi Yanagi, Masahiro Hirano, and Hideo Hosono, J. Am. Chem. Soc. **130**, 14428 (2008).
[12] Yun-Lei Sun, Hao Jiang, Hui-Fei Zhai, Jin-Ke Bao, Wen-He Jiao, Qian Tao, Chen-Yi Shen, Yue-Wu Zeng, Zhu-An Xu, and Guang-Han Cao, J. Am. Chem. Soc. **134**, 12893 (2012).
[13] Ni Ni, Jared M. Allred, Benny C. Chan, and Robert J. Cava, Proc. Natl. Acad. Sci. USA **108**, E1019 (2011).
[14] Jiangang Guo, Shifeng Jin, Gang Wang, Shunchong Wang, Kaixing Zhu, Tingting Zhou, Meng He, and Xiaolong Chen, Phys. Rev. B **82**, 180520(R) (2010).
[15] Y. J. Uemura, Phys. C (Amsterdam) **282–287**, 194 (1997).
[16] R. J. Cava, H. W. Zandbergen, J. J. Krajewski, T. Siegrist, H. Y. Hwang, and B. Batlogg, J. Solid State Chem. **129**, 250 (1997).
[17] Joachim W. Kaiser and Wolfgang Jeitschko, Z. Naturforsch. **57b**, 165 (2002).
[18] A. C. Larson and R. B. Von Dreele, Los Alamos National Laboratory Report LAUR No. 86 (unpublished).
[19] R. D. Shannon, Acta Crystallogr., Sect. A: Cryst. Phys., Diffr., Theor. Gen. Crystallogr. **32**, 751 (1976).
[20] T. Klimczuk, T. M. McQueen, A. J. Williams, Q. Huang, F. Ronning, E. D. Bauer, J. D. Thompson, M. A. Green, and R. J. Cava, Phys. Rev. B **79**, 012505 (2009).
[21] Kenji Ishida, Yusuke Nakai, and Hideo Hosono, J. Phys. Soc. Jpn. **6**, 062001 (2009).
[22] Yongkang Luo, Jinke Bao, Chenyi Shen, Jieke Han, Xiaojun Yang, Chen Lv, Yuke Li, Wenhe Jiao, Bingqi Si, Chunmu Feng, Jianhui Dai, Guanghan Cao, and Zhu-an Xu, Phys. Rev. B **86**, 245130 (2012).
[23] R. E. Walline and W. E. Wallace, J. Chem. Phys. **42**, 604 (1965).
[24] M. T. Fernandez-Diaz, J. Rodriguez-Carvajal, J. L. Martinez, G. Fillion, F. Fernandez, and R. Saez-Puche, Z. Phys. B: Condens. Matter **82**, 275 (1991).
[25] La Blanchetais and Charlotte Henry, J. Recherches Centre Natl. Recherche Sci., Labs. Bellevue (Paris) **29**, 103 (1954).
[26] Jiakui K. Wang, Shan Wu, Collin Broholm, and E. Morosan (unpublished).
[27] J. N. Reimers, J. E. Greedan, R. K. Kremer, E. Gmelin, and M. A. Subramanian, Phys. Rev. B **43**, 3387 (1991).
[28] D. Mikhailova, B. Schwarz, A. Senyshyn, A. M. T. Bell, Y. Skourski, H. Ehrenberg, A. A. Tsirlin, S. Agrestini, M. Rotter, P. Reichel, J. M. Chen, Z. Hu, Z. M. Li, Z. F. Li, and L. H. Tjeng, Phys. Rev. B **86**, 134409 (2012).
[29] Bayrammurad Saparov, Stuart Calder, Balazs Sipos, Huibo Cao, Songxue Chi, David J. Singh, Andrew D. Christianson, Mark D. Lumsden, and Athena S. Sefat, Phys. Rev. B **84**, 245132 (2011).
[30] H. Schweitzer and G. Czycholl, Phys. Rev. Lett. **67**, 3724 (1991).
[31] Elbio Dagotto, *Nanoscale Phase Separation and Colossal Magnetoresistance* (Springer, Berlin, 2003).
[32] Eve J. Wildman, Janet M. S. Skakle, Nicolas Emery, and Abbie C. Mclaughlin, J. Am. Chem. Soc. **134**, 8766 (2012).
[33] N. Emery, E. J. Wildman, J. M. S. Skakle, A. C. Mclaughlin, R. I. Smith, and A. N. Fitch, Phys. Rev. B **83**, 144429 (2011).
[34] A. J. Bray, Phys. Rev. Lett. **59**, 586 (1987).
[35] Robert B. Griffiths, Phys. Rev. Lett. **23**, 17 (1969).
[36] M. E. Fisher, Philos. Mag. **7**, 1731 (1962).
[37] http://pd.chem.ucl.ac.uk/pdnn/peaks/others.htm.
[38] K. Binder and A. P. Young, Rev. Mod. Phys. **58**, 801 (1986).
[39] J. A. Mydosh, *Spin Glasses: An Experimental Introduction* (Taylor and Francis, London, 1993).
[40] A. K. Bera and S. M. Yusuf, Phys. Rev. B **86**, 024408 (2012).
[41] S. K. Malik, W. E. Wallace, and R. Vijayaraghavan, Phys. Rev. B **19**, 1671 (1979).
[42] T. S. Zhao, X. C. Kou, R. Grössinger, and H. R. Kirchmayr, Phys. Rev. B **44**, 2846 (1991).
[43] M. El-Hagary, H. Michor, and G. Hilscher, Phys. B (Amsterdam) **284–288**, 1489 (2000).